Generating a 2-km, all-sky, hourly land surface temperature product from Advanced Baseline Imager data

Aolin Jia[a], Shunlin Liang[a,*], and Dongdong Wang[a]

[a] Department of Geographical Sciences, University of Maryland, College Park, MD, 20742, USA

*Correspondence to: Shunlin Liang (sliang@umd.edu)

Abstract

By characterizing high-frequency surface thermal dynamics at a medium spatial scale, hourly land surface temperatures (LST), retrieved from geostationary satellite thermal infrared (TIR) observations, shows great potential to be used across a range of scientific applications; however, cloud cover typically leads to data gaps and degraded retrieval accuracy in TIR LST products, such as the official Advanced Baseline Imager (ABI) LST product. Studies have focused on the LST gap reconstruction; however, most interpolation-based methods only work for a short-term cloud duration and are unable to adequately compensate for cloud effects, and traditional surface energy balance (SEB)-based methods are able to handle cloud coverage while they are not feasible for use at night. Moreover, few studies have concentrated on recovering the abnormal retrievals of partial cloud pixels. In this study, an all-sky diurnal, hourly LST estimation method based on SEB theory was proposed; the proposed method involved three major steps: 1) an original spatiotemporal dynamic model of LST was constructed from ECMWF Reanalysis *v*.5 (ERA5); 2) clear-sky ABI LST was then assimilated to the dynamic model to generate a continuous LST series; 3) the diurnal cloud effects were superimposed on cloudy time estimated by an innovative optimization method from satellite radiation products. A 2-km, all-sky, hourly LST product was produced over the contiguous US and Mexico from July 2017 to June 2021. Validation was conducted using ground measurements at 18 sites from Surface Radiation (SURFRAD) and core AmeriFlux networks, and produced an overall root-mean-square error (RMSE) of 2.44 K, a bias of -0.19 K, and an R^2 of 0.97 based on 408,300 samples. For clear-sky samples, the RMSE values were 2.37 and 2.24 K for day and nighttime, respectively, which was a notable improvement over the corresponding values of the official ABI LST product (2.73 and 2.86 K, respectively). The RMSE values on cloudy-sky were 2.78 and 2.23 K for day and nighttime, respectively. The daily mean LST by aggregating all-sky, hourly LST had an RMSE of 1.13 K and R^2 of 0.99. Overall, this product showed reliability under consistent cloud durations, although it was slightly affected by surface elevation. The diurnal temperature cycle climatology of major land cover types was also characterized. The product is freely available at: http://glass.umd.edu/allsky_LST/ABI/.

Keywords: land surface temperature, all-sky, diurnal temperature cycle, surface energy balance, ABI, data assimilation

1. Introduction

The Intergovernmental Panel on Climate Change (IPCC) Sixth Assessment Report (AR6) confirmed that the earth's climate has warmed 1.5 °C above pre-industrial levels, in a process unequivocally resulting from human activities (Delmotte et al., 2018; Delmotte et al., 2021). Land surface temperature (LST) drives the surface radiation and hydrological budgets, and is one of the most important indicators for characterizing global climate change (Jia et al., 2020; Jin, 2004; Li et al., 2013; Liang et al., 2021). This radiative temperature at the terrestrial surface reflects the surface equilibrium state, and hence, has been utilized for a variety of purposes, including air temperature and heat flux estimates (Chen and Liu, 2020; Rao et al., 2019), drought monitoring

(Karnieli et al., 2010), permafrost mapping (Zou et al., 2017), urban heat island analysis (Hrisko et al., 2020; Imhoff et al., 2010), and hazard risk detection (e.g., earthquakes, forest fire danger, and parasites) (Blackett et al., 2011; Chuvieco et al., 2004; Neteler et al., 2011). Given the spatiotemporal scale of such research and heterogeneity of LST, satellite remote sensing has become the only feasible approach for measuring regional and global LST.

LST is well retrieved from thermal infrared (TIR) sensors onboard polar-orbiting platforms, such as the Moderate Resolution Imaging Spectroradiometer (MODIS) on both Terra and Aqua (Wan and Dozier, 1996; Wan and Li, 1997); however, because of the limited return times, MODIS LST products cannot capture diurnal temperature cycles (DTCs). DTCs identify the high temporal variability of LST, and play a vital role in advancing meteorological modeling (Orth et al., 2017), downscaling (Zakšek and Oštir, 2012), and intra-day health exposure assessments from extreme temperature events (Hrisko et al., 2020; Jiang et al., 2015). Studies have also revealed that DTCs are influenced by plant stomatal closure; therefore, they can also be used to estimate plant water stress and evapotranspiration levels (Fensholt et al., 2011; Stisen et al., 2008). In addition, the morning warming rate has been shown to be directly related to soil moisture status (Anderson et al., 2007; Piles et al., 2016; Van de Griend et al., 1985). Hence, geostationary (GEO) satellites such as Geostationary Operational Environmental Satellites (GOES)-R Advanced Baseline Imager (ABI) (Yu et al., 2008), Meteosat Second Generation (MSG) Spinning Enhanced Visible and InfraRed Imager (SEVIRI) (Freitas et al., 2009), and the Feng Yun meteorological satellites (Tang et al., 2008), have become an optimal choice for observing sub-hourly LST across a wide spatial coverage (Freitas et al., 2013).

However, cloud cover results in invalid pixels or degraded retrieval accuracy due to partial cloud contamination, constricting LST applications, and limiting all-sky GEO LST products available to the public. Therefore, LST-related analyses have focused strictly on clear-sky cases (e.g., estimating urban air temperature from GOES-16 LST, Hrisko et al. (2020)), or post-processing local temperature data by researchers (e.g., detecting coastal upwelling in the Mid-Atlantic Bight from gap-filled GOES-16 SST by DINEOF, Murphy et al. (2021)). Consequently, there is an urgent need for an all-sky, hourly LST product using a more practical cloudy-sky GEO LST estimation method. Different algorithmic methods have been developed to recover cloudy pixel data in LST products (Mo et al., 2021; Wu et al., 2021), such as passive microwave (PMW) data (Duan et al., 2017; Xu and Cheng, 2021; Yoo et al., 2020; Zhang et al., 2021), modeled data (Fu et al., 2019; Li et al., 2021; Long et al., 2020), mathematical interpolation (Neteler, 2010; Zhang et al., 2022; Zhou et al., 2017), and surface energy balance (SEB) (Jia et al., 2021; Zeng et al., 2018). Although these proposed LST reconstruction methods are sensor-independent, they are primarily designed for polar-orbiting satellites, and directly applying these methods to GEO LST is not efficient and does not take adequate advantage of its higher temporal resolution. In comparison, cloudy-sky GEO LST estimation methods have not been well developed.

Limited studies have utilized PMW data for cloudy-sky GEO LST estimation because of its low spatiotemporal resolutions, in addition to the inherent physical property limitations of microwave signals. Generally, LSTs have considerable diurnal variation, while global PMW data can only be collected twice daily. Moreover, microwave signals are sensitive to surface emissivity, which can be highly affected by soil composition, moisture, and vegetation type; thus, the achieved accuracies of PMW-derived LST vary by up to 6 K (Dash et al., 2002). Marullo et al. (2010) generated gap-free, sea surface temperature (SST) data every 3 h by merging SSTs from the Advanced Microwave Scanning Radiometer (AMSR) PMW and SEVIRI via optimal interpolation, under the assumption that the SST biases at the overlapping passing times remained constant. Such an assumption might be feasible for SSTs because of their relative spatiotemporal stability but would not hold for LSTs. As precipitation has been successfully retrieved via a combination of PMW and GEO data assimilation (Kidd et al., 2003; Ushio et al., 2009), PMW data still maintain the potential for cloudy-sky GEO LST estimates (Holmes et al., 2015; Wu et al., 2021).

Simulated LSTs by land surface models are another auxiliary data candidate for filling cloud gaps because of their continuous spatial coverage and high temporal resolution. Marullo et al. (2014) fused clear-sky SSTs from the SEVIRI and Mediterranean Forecasting System to generate gap-free, hourly SSTs using diurnal optimal interpolation across a moving temporal window. Different model outputs have also been evaluated for filling invalid SST pixels (Nardelli et al., 2015); however, the resulting accuracies of cloudy-sky results were highly reliant upon simulation data, especially for continuous cloudy days, and no further correction was implemented (Fablet et al., 2017). Dumitrescu et al. (2020) fused daytime hourly SEVIRI LSTs and modeled skin temperature using multiple linear regression and generalized additive models, in addition to elevation, time, and solar radiation to improve GEO LST estimation under clouds. Inherently, applying a clear-sky statistical model to cloudy cases introduces error, as the cloud cooling effect cannot be replicated by cloud-free samples. In addition, surface parameters (e.g., albedo and vegetation coverage) also substantially influence LST, but have not been adequately accounted for. Furthermore, few studies have focused on recovering ABI LST by combining satellite retrieval with model simulations.

Owing to the unique cycles, temporal interpolation based on a DTC model is the dominant method for missing GEO LST reconstruction. A DTC model is defined by a harmonic function during the day and an exponential function at night (Duan et al., 2012), of which parameters can be obtained by model simulation (Jin and Treadon, 2003), statistics (Aires et al., 2004; Ignatov and Gutman, 1999), and physical interpretation (Göttsche and Olesen, 2009; Schädlich et al., 2001). Parton and Logan (1981) initially created a DTC model to describe real-time temperature variation, which was then developed for GEO brightness temperature (BT) or LST temporal interpolation (Göttsche and Olesen, 2001; Inamdar and French, 2009; Inamdar et al., 2008; Jiang et al., 2006; Udahemuka et al., 2008; Van den Bergh et al., 2007). Thereafter, DTC models were improved by introducing energy partitioning constraints (Gottsche and Olesen, 2009; Zhan et al., 2013; Zhan et al., 2014), and Huang et al. (2014) proposed a generic, quasi-physical DTC framework based on the SEB and heat conduction equations. Studies have also attempted to increase feasibility by reducing the quantity of DTC model parameters (Duan et al., 2014; Holmes et al., 2013), or including additional data (e.g., spatially adjacent LST pixels or monthly mean) (Quan et al., 2014; Quan et al., 2018; Zhou et al., 2013). Accuracies and feasibilities of different DTC models have been comprehensively evaluated and summarized by Duan et al. (2012) and Hong et al. (2018).

DTC-based models have clear mathematical formulas and are easily applicable; however, the equations cannot be resolved if enough clear-sky observations ($\geqslant$4) per day are not available. Liu et al. (2017b) increased the clear-sky samples available to the DTC model by combining it with a spatial inverse distance-weighted interpolation; however, such interpolation methods are unreliable when cloud coverage has large spatiotemporal scales (Vinnikov et al., 2008). In addition, DTC models determine interpolation accuracy, although model selection is difficult for various study areas. Accordingly, Wu et al. (2019) utilized a convolutional neural network (CNN) to reconstruct the missing GEO LSTs from spatiotemporally adjacent pixels, a functional approach for larger missing regions. Some other spatiotemporal interpolation methods were also designed for GEO LSTs, such as reproducing kernel Hilbert space (RKHS) interpolator (Van den Bergh et al., 2007), multi-channel singular spectrum analysis (M-SSA) (Ghafarian et al., 2012), data interpolating empirical orthogonal functions (DINEOF) (Beckers et al., 2014), and Fourier functions (Liu et al., 2017a). Ultimately, all spatiotemporal interpolation methods are affected by terrain complexity and referenced clear-sky pixels' distributions, as well as fill gaps with hypothetical "clear-sky" LSTs; however, cloud cooling (warming) effects on LST during the daytime (nighttime) cannot be ignored (Ermida et al., 2019). In addition, few studies have tested spatiotemporal interpolation methods using the ABI LST.

Considering the straightforward physical process, the SEB-based method represents one of the most promising solutions for cloudy-sky GEO LST estimation. Jin (2000) proposed an SEB-based method containing two primary steps: 1) reconstruct hypothetical LSTs based on neighboring observed pixels, and 2) superpose the cloud effect corrections estimated from surface insolation, air temperature, wind speed, and other variables. Essentially, it uses an interpolation method before correcting the interpolated LSTs to realistic cloudy-sky LSTs based on SEB. Lu et al. (2011) adjusted the algorithm for SEVIRI LST by utilizing only the temporal series. A combined diurnal cycle model of downward solar radiation (DSR) was designed to reconstruct hypothetical LST values (Zhang et al., 2015b); however, the previous SEB-based methods remain restricted by the limitations of interpolation and only work when there are sufficient nearby clear-sky observations. In addition, local meteorological parameters are required, which considerably limits their feasibility over larger spatial scales. More importantly, traditional SEB-based methods were driven by DSR, implying that the nighttime all-sky LST could not be obtained. The SEB-based method was also tested by Feng Yun-2D GEO LSTs, and a continuous DTC series was generated assuming negligible nighttime cloud effects (Zhang et al., 2017). A revised SEB algorithm was developed by Martins et al. (2019) for SEVIRI LST, where an iteration method was employed by adjusting LST and turbulent heat fluxes to meet SEB during periods of cloud cover, of which parameterization schemes of turbulent heat fluxes and radiation components were from MSG/SEVIRI Satellite Application Facility on Land Surface Analysis (LSA-SAF) product suite; however, heat flux estimation generally has higher uncertainty than LST retrieval, and thus in SEB fitting step, the iteratively adjusted cloudy-sky LSTs could be affected by initial value and heat fluxes' accuracy.

Furthermore, previous studies have rarely discussed pixel recovery and algorithm robustness toward cloud-contaminated pixels. Partially cloud-covered pixels can be retrieved, albeit with substantial bias (Ma et al., 2020; Yang et al., 2019), and accidentally interpolating or fusing contaminated pixels will introduce significant uncertainty to the filled results, thereby restricting the application of the current cloudy-sky GEO LST estimation algorithms.

Jia et al. (2021) estimated the cloudy-sky Visible Infrared Imaging Radiometer Suite (VIIRS) LSTs by assimilating the noon clear-sky retrievals to a temporal LST evolving model, and simulated LSTs on cloudy days were corrected from satellite radiation products based on SEB. By considering the importance and the scarcity of the all-sky GEO LST, here, the preliminary algorithm was further refined to generate an all-sky, hourly LST product from GOES-16 ABI in pursuit of three primary objectives: 1) design an innovative spatiotemporal dynamic model and assimilation scheme to increase algorithm robustness and take full advantage of the high temporal resolution of ABI LST data; 2) propose a novel, diurnal cloud effect estimation method that can recover complete DTCs, and calculate accurate daily mean LSTs; and 3) effectively recover abnormally-retrieved LSTs mainly caused by partial cloud coverage. The first 2-km, all-sky, hourly LST product was produced from July 2017 to June 2021, and it was comprehensively assessed over the contiguous US (CONUS) and Mexico.

2. Data and methods

2.1 Data

This study assimilated the official ABI LSTs into a spatiotemporal dynamic model constructed by European Centre for Medium-range Weather Forecasts (ECMWF) Reanalysis v.5 (ERA5), and the cloud effects were primarily estimated by satellite products from ABI, Clouds and Earth's Radiant Energy Systems (CERES), MODIS, and Global LAnd Surface Satellite (GLASS). Eighteen ground sites from the Surface Radiation (SURFRAD) and core AmeriFlux networks were used for ground validation. Further information is provided below, where the basic input data are listed in Table 1, and the site metadata are presented in Table 2.

2.1.1 Satellite and reanalysis products

The official National Oceanic and Atmospheric Administration (NOAA) GOES-16 ABI LST was considered the target for all-sky diurnal LST estimates, while the GOES-16 ABI DSR and cloud top temperature (CTT) were used to calculate the diurnal cloud radiative effect (CRE). GOES-16 was launched in November 2016, and its LST product was retrieved using a split-window method (Yu and Yu, 2018). The longest set of NOAA ABI LSTs was available from mid-2017; thus, the all-sky diurnal LST from July 1, 2017, was released. It provides 10-km hourly LST over North and South America (full disk), and 2-km hourly data (selected for the present study) covering the CONUS and Mexico. The GOES-16 ABI LST reached its provisional maturity in March 2018, achieving stable accuracy based on site validation (Yu et al., 2018). The GOES-16 ABI DSR product combines forward and backward algorithms to estimate reflection and transmission, accounting for all major interactions of radiation between the atmosphere and surface. Both the visible and infrared channels were utilized with other inputs (e.g., albedo and atmospheric composition) to retrieve surface DSR (Laszlo et al., 2020). The NOAA officially released GOES-

16 ABI CTT (Heidinger et al., 2010; Heidinger et al., 2020) is retrieved simultaneously with cloud top height and pressure for each cloudy pixel, using an analytical model of infrared radiative transfer embedded into an optimal retrieval methodology. The ABI observations for bands at 11, 12, and 13.3 μm were used to characterize cloud microphysical information. CTT was utilized to estimate cloudy-sky downward longwave (DLW) radiation, and both atmospheric variables (DSR and CTT) were interpolated bilinearly to align with the spatial scale of ABI LST data.

Cloud shortwave net radiative forcing is the difference between all-sky DSR and the theoretical clear-sky DSR, which is essential for the cloud cooling/warming effect estimation, thus theoretical clear-sky DSR on cloudy times is required. The CERES clear-sky DSR product was employed. Specifically, the CERES SYN1-deg product provides hourly, spatiotemporally continuous surface radiation products by retrieving observations from both polar-orbiting and GEO satellites (Kato et al., 2018). Based on the Fu–Liou radiative transfer theory (Fu et al., 1997), the theoretical clear-sky DSR was obtained by removing the cloud impact estimates from multiple data sources, including microwave observations.

The CERES project aims to analyze the radiation budget at atmosphere and surface levels; thus, it retrieves the theoretical clear-sky DSR at cloudy times to estimate CRE. We directly take advantage of the CERES clear-sky DSR product, but use GOES-16 all-sky DSR rather than CERES all-sky DSR because the former has a higher spatial resolution. As clear-sky DSR has limited spatial heterogeneity, CERES clear-sky DSR was downscaled by bilinear interpolation.

Auxiliary input satellite data, such as a digital elevation model (DEM), were used for modeled LST downscaling (Danielson and Gesch, 2011). The VIIRS all-sky broadband emissivity (BBE) product was used to estimate the modeled clear-sky LST series, and was spectrally adjusted from the historical Advanced Spaceborne Thermal Emission and Reflection Radiometer Global

Emissivity Dataset (ASTER-GED) and MODIS land surface emissivity product (Wang et al., 2019). Cloudy pixels were replaced by the mean value of available adjacent grids within 2.5° of the same surface type. MODIS land cover data (MCD12Q1) (Sulla-Menashe and Friedl, 2018) were used to select similar pixels in a spatial window, and aggregated (water, forest, low vegetation, urban, and ice/snow) to increase classification accuracy. MODIS albedo (Schaaf et al., 2002) has been widely employed in SEB-related studies (He et al., 2014; Jia et al., 2020). Here, surface albedo was used for shortwave CRE calculation after a bilinear interpolation in cloudy time, and it was assumed that values would remain relatively stable in the neighboring days. The all-sky GLASS leaf area index (LAI) was utilized for estimating energy partitioning (Liang et al., 2021). All auxiliary data have a higher spatial resolution, and thus, have been aggregated to 2 km to match the dominant spatial scale used.

ERA5 (Hersbach et al., 2020) provides simulated hourly, clear-sky DLW and upward longwave (ULW) radiation for creating a clear-sky LST dynamic model, in addition to providing column water vapor (CWV) for DLW parameterizations. Clear-sky DLW and ULW were simulated by ERA5 for the same atmospheric and meteorological conditions as the corresponding representative scenario, but assuming clouds were absent. The all-sky ERA5 skin temperature was not used here, as reanalysis datasets primarily involve simulated clouds (Wang and Dickinson, 2013). The metadata for all input information are summarized in Table 1.

Table 1. Metadata for all-sky diurnal LST input.

Product	Variable	Spatial resolution	Temporal resolution	Usage
ABI	LST	2-km	hourly	clear-sky GEO LST
ERA5	clear-sky DLW and ULW	0.25°	hourly	LST dynamic model

VIIRS	BBE	1-km	daily	LST dynamic model, longwave CRE
GMTED2010	DEM	1-km	-	downscaling
MODIS	land cover type	500-m	yearly	neighboring pixel selection
ABI	DSR	0.25°	hourly	shortwave CRE
CERES	clear-sky DSR	1°	hourly	shortwave CRE
MODIS	surface albedo	500-m	daily	shortwave CRE
ABI	CTT	2-km	hourly	longwave CRE
ERA5	CWV	0.25°	hourly	longwave CRE
GLASS	LAI	500-m	daily	energy partitioning

In addition, in order to demonstrate the advancement of the proposed all-sky diurnal LST, we also included two available all-sky skin temperature reanalysis datasets for accuracy comparison. As there were no available satellite-derived all-sky hourly LSTs over the CONUS before this study, skin temperatures from ERA5-Land and North American Land Data Assimilation System (NLDAS) were employed and validated by sites at different hours of a day for accuracy comparison. ERA5-Land replays of the land component of the ERA5 climate reanalysis with a finer spatial resolution (0.1°) at an hourly scale. NLDAS aims to provide spatially and temporally consistent land surface model datasets by reanalyzing observations to support modeling activities. GOES surface brightness temperature is considered the essential forcing data (Pinker et al., 2003). Hourly skin temperature with 0.125° resolution from the NLDAS Noah model has been chosen in this study. Both reanalysis skin temperature data were downscaled to 2 km based on elevation (Duan et al., 2017).

2.1.2 Ground measurements

Comprehensive validation using ground-based measurements is essential for the assessment and application of diurnal LST products. As widely distributed sites can encompass different climates and land cover types, 18 *in situ* sites from the SURFRAD (7) and core

AmeriFlux (11) networks were employed for the all-sky diurnal LST validation. SURFRAD was established in 1993 through the support of the NOAA's Office of Global Programs, with an aim to provide climate research with precise, continuous, long-term ground references of the surface radiation records over the US (Augustine et al., 2000). It has been commonly utilized for surface radiation product assessment (Jiang et al., 2018; Zeng et al., 2020; Zhou et al., 2018), and was thus selected here to validate the SEB accuracy from satellite-based estimates. Core AmeriFlux sites are flux towers providing timely, high-quality, and continuous data, with the basic objective to ensure high-resolution data collection across a broad range of ecosystems and locations in the US. The sites utilized here included ULW and DLW observations (AmeriFlux, 2021), and ground measured LSTs were computed using ULW, DLW, and all-sky VIIRS BBE by Eq. 1 in Jia et al. (2021), based on the Stefan–Boltzmann law. The site location map can be seen in Figure 1, with site details listed in Table 2.

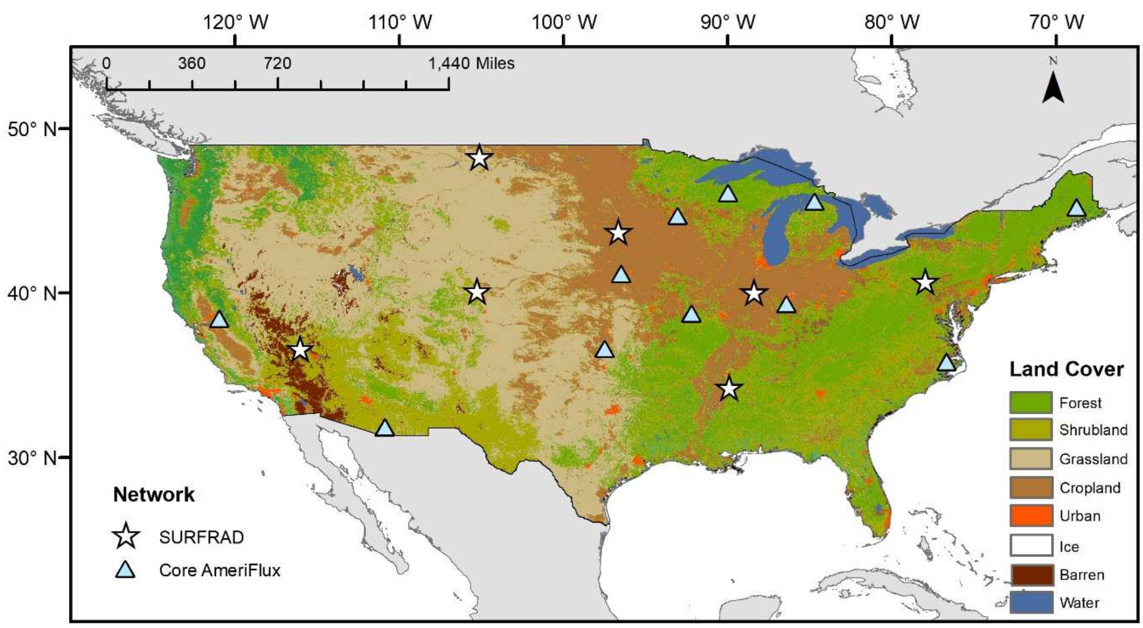

Figure 1. Distribution of the 18 sites with landcover types from Surface Radiation (SURFRAD) and Core AmeriFlux networks.

282 **Table 2.** Metadata for the *in situ* sites.

No.	Name	Lat. (°)	Long. (°)	Elev. (m)	Land cover	Period
1	BND	40.0519	-88.3731	230	cropland	2018–2021
2	FPK	48.3078	-105.1017	634	grassland	2018–2021
3	GWN	34.2547	-89.8729	98	pastureland	2018–2021
4	DRA	36.6237	-116.0195	1007	arid shrubland	2018–2021
5	PSU	40.7201	-77.9309	376	cropland	2018–2021
6	SXF	43.7340	-96.6233	473	grassland	2018–2021
7	TBL	40.1250	-105.2368	1689	grass and shrub	2018–2021
8	US-ARM	36.6058	-97.4888	314	cropland	2018–2021
9	US-Ho1	45.2041	-68.7402	60	forest	2018–2020
10	US-Los	46.0827	-89.9792	480	wetland	2018–2021
11	US-MMS	39.3232	-86.4131	275	forest	2018–2021
12	US-MOz	38.7441	-92.2000	219	forest	2018–2019
13	US-NC2	35.8030	-76.6685	5	forest	2018–2020
14	US-NE1	41.1651	-96.4766	361	cropland	2018–2020
15	US-Ro5	44.6910	-93.0576	283	cropland	2018–2021
16	US-SRM	31.8214	-110.8661	1120	woody savannas	2018–2021
17	US-Ton	38.4309	-120.9660	177	woody savannas	2018–2020

18	US-UMB	45.5598	-84.7138	234	forest	2018–2020

Site observations with low-quality flags in the raw records were filtered out during preprocessing. SURFRAD sites have a 1-min temporal resolution, and the raw ground observations were extracted and averaged within a 15-min time window, centered on the satellite recording time. Core AmeriFlux sites have a 30-min temporal resolution, and only the site samples within the 15-min time window of satellite data acquisition were utilized for validation. Bias, root-mean-square error (RMSE), and the coefficient of determination (R^2) were the validation indices used. The validation samples were extracted from the site locations, and sample accuracies of diurnal all-sky LSTs and GOES-16 LSTs were compared during daytime and nighttime, from July 2018 to June 2021 after GOES-16 reached provisional maturity (Yu et al., 2018). As only SURFRAD sites have 1-min observations, they were employed for daily mean LST validation. In addition, only high-quality ground measurements that were fully observed (24×60 high-quality records in a day) were averaged to obtain the daily mean references.

2.2 Framework

The conceptual flowchart of the proposed SEB-based, all-sky, hourly LST estimation method is shown in Figure 2; it can be divided into three primary steps: 1) an original spatiotemporal dynamic model of LST was constructed from ERA5 data; 2) after cleaning likely cloud-contaminated pixels, continuous LST series were reconstructed by assimilating the official clear-sky ABI LST to the dynamic model from spatial and temporal dimensions; and 3) diurnal cloud effects were superimposed on cloudy time estimated by an innovative optimization method from satellite radiation products.

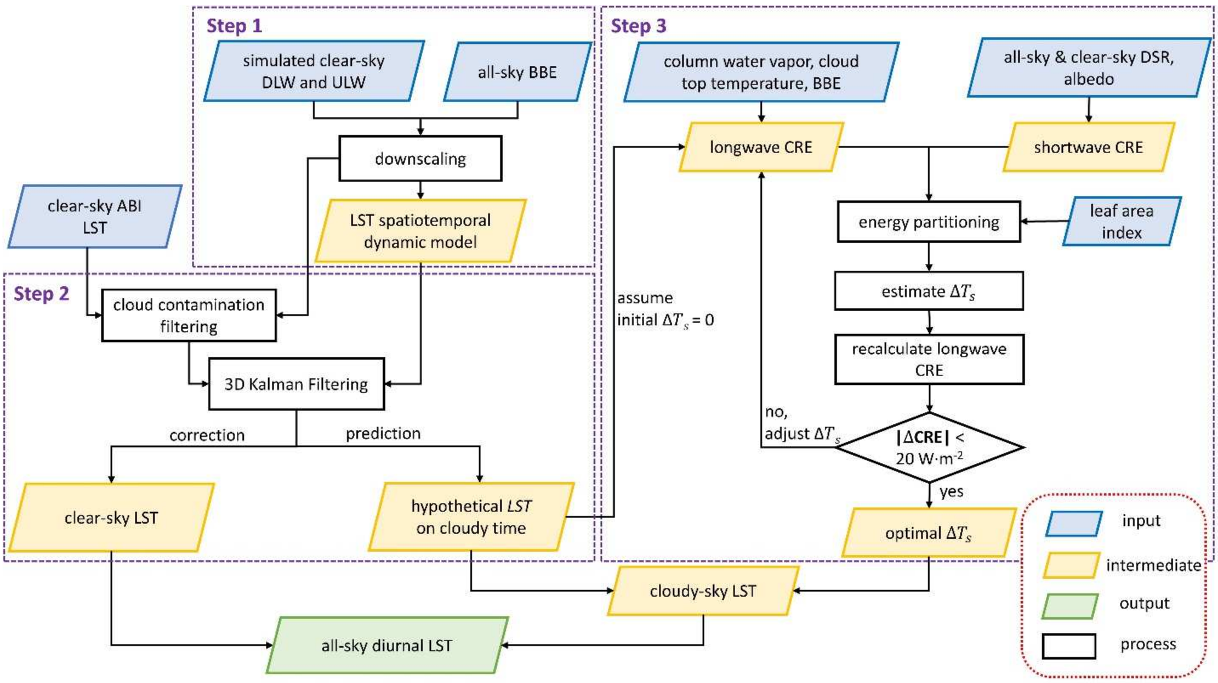

Figure 2. Flowchart of the all-sky, hourly land surface temperature (LST) product generation from the Advanced Baseline Imager (ABI) data: DLW, downward longwave radiation; DSR, downward shortwave radiation; ULW, upward longwave radiation; CRE, cloud radiative effect; BBE, broadband emissivity; and ΔT_s, cloud effects on LST.

In the first step, a clear-sky LST dynamic model was built from ERA5 using a 3-D Kalman filter (KF). ERA5 released the simulated clear-sky ULW and DLW radiations, which are used for computing clear-sky LST combined with all-sky BBE (Wang et al., 2019). After downscaling, a spatiotemporal dynamic model was constructed for each pixel location using the simulated LST series (Section 2.3). Continuous simulations in clear-sky conditions rather than directly modeled skin temperatures were used in this study because the realistic cloud effects from the available radiation satellite products were superposed in the final step. ERA5 clear-sky fluxes are simulated by the real atmospheric condition so that they can still provide the LST variation signals caused by near-surface meteorological changes (e.g., advective cold air movement).

In the second step, continuous LSTs were obtained by assimilating the official ABI LST to the dynamic model. Before the assimilation, a partially cloud-contaminated pixel was identified when: 1) its absolute difference with the corresponding simulated LST was significantly larger (three standard deviations) than other days within ±15 days, and 2) surrounding cloudy pixels were >50% of the spatial window. Detected likely cloud-contaminated pixels were masked to be recovered. Subsequently, clear-sky ABI LSTs within a spatial window were assimilated into the spatiotemporal dynamic model to correct the simulation (Section 2.4). After processing the prediction from the corrected results, hypothetical clear-sky LSTs were reconstructed for missing or likely cloud-contaminated pixels.

In the third step (Section 2.5), shortwave CRE was acquired from current land surface albedo and clear-sky/all-sky DSR satellite products. Estimating longwave CRE required cloudy-sky LST that is unavailable; therefore, it was assumed that the initial cloud effects (ΔT_s) were 0 K, and the hypothetical LST was used for the initial CRE calculation. By converting total CRE to the cloud heat effect after energy partitioning, an updated ΔT_s was calculated, and the longwave CRE was recomputed. To reduce the difference between the CREs of the two loops, ΔT_s was adjusted and iteratively reprocessed using the previous steps until the SEB was balanced. Subsequently, optimal ΔT_s was obtained and used to correct the hypothetical LST during cloudy periods. All-sky diurnal LST was the combination of clear-sky LST in the second step and the estimated cloudy-sky LST in the third step.

2.3 Spatiotemporal dynamic model

An original spatiotemporal dynamic model was designed to spatiotemporally characterize the simulated clear-sky LST dynamics around a target pixel. The simulated clear-sky LST was calculated from the ERA5 clear-sky longwave radiations and all-sky BBE (Wang et al., 2019), according to the Stefan–Boltzmann law (Liang et al., 2010). To match the spatial scale, the simulated LST was preliminarily downscaled to 2-km using elevational information (Duan et al., 2017), and the resulting spatiotemporal dynamic model was built within a 150-km spatial window, centered on the target pixel (see Section 3.1), which can be mathematically represented as follows (Eqs. 1–4):

$$LST_{c,t,d}^{t} = F_{c,t,d}^{t} \times LST_{c,t,d-1}^{t}, \quad (1)$$

$$F_{c,t,d}^{t} = 1 + \frac{1}{Z_{c,t,d} + \delta}, \quad (2)$$

$$LST_{c,t,d}^{s} = \sum_{1}^{N} w_{m,d} \cdot \left(F_{m,t,d}^{s} \times LST_{m,t,d}^{s}\right), \quad (3)$$

$$F_{m,t,d}^{s} = 1 + \frac{1}{Z_{m,t,d} + \delta}, \quad (4)$$

The aforementioned equations hold true for target center pixel *c,* at time *t* (defined by the UTC coordinate) of day *d*. The spatiotemporal dynamic model includes a temporal module ($F_{c,t,d}^{t}$; Eqs. 1 and 2) and a spatial module ($F_{c,t,d}^{s}$; Eqs. 3 and 4). $LST_{c,t,d}^{t}$ represents the prediction of the temporal module, which is estimated from $LST_{c,t,d-1}^{t}$, i.e., the LST 24 h before, as the data in the modeled series are most closely related to the same time on different days (TOD) (Marullo et al., 2014); thus, samples at the same TOD generally have similar simulated uncertainties, allowing for corrections made by data assimilation to be easily passed on to the following days. $Z_{c,t,d}$ is the difference between the simulated LSTs at *t* of *d* and *d*-1, and setting δ = 0.01 avoids a null denominator. $LST_{c,t,d}^{s}$ is the weighted average prediction from pixels of adjacent grids at time *t* of day d (Eqs. 3, 4). $Z_{m,t,d}$ represents the simulated LST difference between center c and one adjacent pixel m. The spatial module ($F^{s}_{m,t,d}$) is activated only when there are valid neighboring ABI LSTs; moreover, only the surrounding pixels with the same land cover as c were utilized for calculating $LST^{s}_{c,t,d}$, to minimize the bias caused by land cover differences (Nogueira et al., 2021). The MODIS land cover data (MCD12Q1) were aggregated (water, forest, low vegetation, urban, and ice/snow) to increase the classification accuracy. Therefore, the total number N equals the available clear-sky ABI pixels with the same land cover in the window, and the weight w was determined by the relative magnitude of inverse distance between each spatially adjacent pixel and c. The spatiotemporal dynamic model was constructed with relative variation information of the simulated LST, rather than the absolute magnitude, because the difference series can remove the bias and keep the important dynamic modeling signals (Hong et al., 2021).

Before data assimilation is implemented, likely cloud-contaminated ABI LSTs need to be masked. It was assumed that the simulation might have higher uncertainty, but the modeling process was stable; thus, when a substantially abnormal difference between satellite retrieval and model simulation appeared near the clustered cloud pixels, it was more likely to be partially contaminated. After the spatiotemporal dynamic model was generated, and likely contaminated observations were removed, clear-sky ABI LSTs were assimilated into the modeling process, and the errors caused by model downscaling and predictions were corrected continuously.

2.4 Data assimilation

KF is a data assimilation tool that uses discontinuous observations to correct model prediction and modeling uncertainty, and ultimately obtains continuous and accurate estimations.

Each correction step is essentially the weighted average based on relative error magnitudes of modeling and observation. For example, in Jia et al. (2021), LST time-evolving models are corrected using satellite clear-sky LST retrievals, and formulate predictions on cloudy time based on the corrected results. However, this preliminary scheme only utilized the temporal information. In this study, A 3D-KF was proposed by revising the temporal KF, and a spatial module was activated when the neighboring ABI LST was observed in a spatial window centered on pixel *c*. Adjacent, simulated LSTs were corrected first by corresponding ABI LSTs, and then LST at *c* were predicted (Eqs. 3, 4). The spatial module helped the temporal module correct the predictions, particularly when there were no observations at *c*, but neighboring ABI LSTs were available. The temporal module of the 3D-KF was calculated according to Eqs. (5–8):

$$\widehat{LST_d^t}^- = A_{d-1}^t \widehat{LST}_{d-1} + \omega_{d-1}^t, \tag{5}$$

$$\widehat{LST_d^t} = \widehat{LST_d^t}^- + K_d^t(LST_{d,c} - \widehat{LST_d^t}^-), \tag{6}$$

$$K_k^t = P^-{}_d(P^-{}_d + R)^{-1}, \tag{7}$$

$$P_d = (I - K_k^t)P^-{}_d, \tag{8}$$

where $\widehat{LST_d^t}^-$ is the prior estimate of the temporal dynamic model (A_{d-1}^t, representing Eqs. 1, 2) at center *c* on day *d*, from the previous filtered outcome $\widehat{LST}_{d-1}$. A symbol with – above indicates that it is a prior prediction. And then the prediction error ω_{d-1}^t is propagated to $P^-{}_d$. The initial modeling error was calculated by referring to the corresponding ABI LST at *c*, which did not affect the overall accuracy because it is continuously corrected by observations, and the first computation date is one month earlier than the starting date of the released product. $\widehat{LST_d^t}$ is the corrected result by filtering (K_d^t) the prior prediction ($\widehat{LST_d^t}^-$) using the ABI retrieval $LST_{d,c}$ (Eq. 6). The retrieval error covariance *R* was set to 4 (Yu and Yu, 2020; Yu et al., 2019). K_d^t is based on the relative magnitudes of $P^{-}{}_{d}$ and R (Eq. 7), and the prediction uncertainty ($P^{-}{}_{d}$) is then corrected to P_d by K_d^t, and I is a unit matrix (Eq. 8). More details can be found in Jia et al. (2021). The spatial module is mathematically represented by Eqs. (9, 10):

$$\widehat{LST^{s}_{m,d}} = x_{m,d} + K_d^s(LST_{m,d} - x_{m,d}), \tag{9}$$

$$\widehat{LST_d^s}^{-} = \frac{\sum(A_d^s \widehat{LST^{s}_{m,d}} + \omega_d^s)}{N}, \tag{10}$$

Eqs. 9–10 show that spatial KF (K_k^s) was implemented to assimilate surrounding clear-sky retrieval ($LST_{m,d}$) into spatially neighboring simulations ($x_{m,d}$) with simulation error covariance S, and the corrected spatial model prediction $\widehat{LST^{s}_{m,d}}$ was obtained at m with an error ω_d^s. K_k^s is calculated from S and R, similar to Eq. 7. The S was computed by referring to the ABI LSTs in the spatial window and corrected to P_d^s, similar to Eq. 8. The predicted LST at c ($\widehat{LST_d^s}^{-}$ in Eq. 10) was computed by averaging predictions from all $\widehat{LST^{s}_{m,d}}$ in the spatial dynamic model (A_d^s, representing Eqs. 3, 4), where N equals the available retrieved ABI LST, of which the prediction error is P_d^{s-}.

On clear-sky conditions, the filtered LST estimate ($\widehat{LST}_d$) of c on d was the final clear-sky LST output, by averaging the results from the temporal ($\widehat{LST_d^t}$, Eq. 6) and the spatial ($\widehat{LST_d^s}^{-}$, Eq. 10) KF. Weights were based on the relative magnitude of the temporal and spatial module uncertainties (Eq. 11).

$$\widehat{LST}_d = \begin{cases} \frac{P_d^{s-}}{P_d^{s-}+P_d}\widehat{LST_d^t} + \frac{P_d}{P_d^{s-}+P_d}\widehat{LST_d^s}^{-}, & \text{clear} - \text{sky} \\ \frac{P_d^{s-}}{P_d^{s-}+P^{-}{}_{d}}\widehat{LST_d^t}^{-} + \frac{P^{-}{}_{d}}{P_d^{s-}+P^{-}{}_{d}}\widehat{LST_d^s}^{-}, & \text{cloudy} - \text{sky} \end{cases} \tag{11}$$

On cloudy-sky conditions, $\widehat{LST}_d$ is the reconstructed LST on cloudy-sky, the weighted average from predictions from $\widehat{LST_d^t}^-$ (Eq. 5) and $\widehat{LST_d^s}^-$ (Eq. 10). Cloud effect (ΔT_s) correction is required to convert the $\widehat{LST}_d$ to final cloudy-sky LST output: $LST_{\mathrm{cld}} = \widehat{LST}_d + \Delta T_s$. ΔT_s is introduced in Section 2.5.

The dynamic model with KFs was continuously processed for d+1 based on $\widehat{LST}_d$. The continuous LST series was reconstructed by 3D-KF, and the diurnal LST at clear-sky was essentially the weighted spatiotemporal fusion of ABI LSTs and model simulations. Further, the simulations during cloudy periods were also initially revised; however, the generated hypothetical LST required further correction by superposing the cloud effects based on SEB during day and nighttime.

2.5 Diurnal cloud effect

By reflecting the state of energy exchange, LST is an important component of the SEB (Eq. 12):

$$R_n = DSR(1-\alpha) + \varepsilon DLW - \sigma\varepsilon LST^4 = G + LE + H, \quad (12)$$

where R_n is the net radiation, α is the surface albedo, ε is the broadband emissivity (BBE), and σ is the Stefan–Boltzmann constant. The available energy is partitioned into ground heat (G), latent heat (LE), and sensible heat (H), and finally affects LST as the surface response. By following the LSA-SAFs evapotranspiration algorithm (Arboleda et al., 2017), G was estimated by partitioning R_n according to LAI. The energy partitioning parameter is set to 0.15, 0.05, and 0.10 for rocks, snow, and inland water, respectively (Jia et al., 2021). G can also be expressed using the conventional force-restore method (Jin and Dickinson, 2000):

$$G = k_g \frac{\partial T}{\Delta h} = k_g \frac{LST - T_d}{\Delta h}, \quad (13)$$

where k_g is the surface thermal conductivity (W·m^{-1}·K^{-1}), and Δh is the depth of the subsurface layer (0.1 m). By assuming that the subsurface layer temperature (T_d) is insensitive to SEB, Eq. 13 can be revised as follows (Eq. 14):

$$\frac{\partial G}{\partial LST} = \frac{\partial}{\partial LST}\left[k_g \frac{LST - T_d}{\Delta h}\right] \approx \frac{k_g}{\Delta h}, \quad (14)$$

where ∂G can be considered the change in ground heat caused by cloud cover, partitioned from the CRE. Thus, after estimating k_g, the heat change can be converted to the corresponding cloud effect (ΔT_s). Essentially, k_g indicated the local sensitivity of LST response to the SEB. By taking advantage of the high temporal resolution of diurnal LST, a novel method for estimating $k_g$was created (Eq. 15):

$$k_g = \Delta h \frac{\overline{G_{noon}} - \overline{G_{sr}}}{\overline{LST_{noon}} - \overline{LST_{sr}}}, \quad (15)$$

where $\overline{G_{noon}}$ ($\overline{LST_{noon}}$) and $\overline{G_{sr}}$ ($\overline{LST_{sr}}$) are the monthly (±15 days) averaged ground heat (clear-sky LST) at noon and sunrise, respectively. It was assumed that morning warming was primarily due to the radiation budget; the continuous LST series was obtained from data assimilation, and *G* was estimated from clear-sky radiation data with LAI. The monthly mean was utilized because the surface property was assumed to be stable in closing days, while the DTC on any specific day could be disturbed by meteorological conditions; thus, the difference in LSTs in Eq. 15 may be too small to generate k_g accurately. Monthly averaging can therefore remove these disturbances. Clear-sky heat and temperature series were chosen to estimate k_g, as clear-sky LSTs have a clearer response to morning warming influenced by SEB.

Therefore, the primary objective of diurnal cloud effect estimation was to quantify the diurnal CRE. CRE will be estimated by hourly cloudy-sky and clear-sky radiation fluxes in order to quantify the impact toward LST from different cloud conditions. Previous studies aiming to estimate cloudy-sky LST based on SEB have mainly built a linear relationship between DSR and R_n (Jin, 2000; Yu et al., 2014; Zeng et al., 2018). This is because shortwave net radiation is the principal driving factor of daytime R_n (Jiang et al., 2018; Wang and Liang, 2009); however, nighttime cloudy-sky LST cannot be recovered. Instantaneous longwave CRE has historically been difficult to estimate in previous studies, as such cloudy-sky LSTs are a basic parameter. Accordingly, an innovative optimization method was created here to determine the diurnal net CRE by separating the hourly shortwave ($CRE_{short\text{-}net}$) and longwave ($CRE_{long\text{-}net}$) components. $CRE_{short\text{-}net}$ can be easily calculated from surface albedo and the difference of ABI all-sky and CERES clear-sky DSRs [Eq. 9 in Jia et al. (2018)], whereas $CRE_{long\text{-}net}$ needs to be estimated as follows:

$$CRE_{long-net} = (\varepsilon DLW_{cld} - \sigma\varepsilon(LST_r + \Delta T_s)^4) - (\varepsilon DLW_{clr} - \sigma\varepsilon LST_{clr}^4), \quad (16)$$

where LST_r was reconstructed by the data assimilation step, and ΔT_s, DLW_{clr}, and DLW_{cld} were the unknown variables.

Current DLW parameterizations are difficult to apply, as most existing satellite-based algorithms depend on parameters that are not readily accessible from space (Cheng et al., 2019), such as the liquid water path, vapor pressure, and cloud base temperature. To this end, Wang et al. (2020) developed a practical all-sky DLW parameterization scheme that employs available satellite input data. By combining the CERES data, with MODerate resolution atmospheric TRANsmission (MODTRAN) simulations, a global training database with approximately 55,664 records for cloudy-sky, and 62,806 for clear-sky conditions was constructed. This algorithm has been used for hourly, all-sky DLW product generation (Letu et al., 2021). Based on the integrated training samples, the relationship was built using a general parameterization scheme [Eqs. 1 and 2 in Wang et al. (2020)] and a random forest machine-learning scheme, separately. Two methods perform close accuracy, achieving greater levels of RMSE (~22 W·m^{-2}) and feasibility over large regions compared to earlier studies. In the parameterizations, CWV was obtained from ERA5, and official CTT data is released by the GOES-16 product suite.

As cloudy-sky LST is required for calculating longwave radiative effect (Eq. 16), an optimization method is necessary to obtain the best ΔT_s to balance the energy in previous equations. In the initial calculation, ΔT_s was assumed to be 0 K in Eq. 16, and the initial CRE was computed. After partitioning the CRE to ground heat through the LAI, an updated ΔT_s was estimated using a predetermined k_g; thus, the CRE can be recomputed. By iteratively comparing the CRE differences and adjusting ΔT_s (0.05 K in each iteration), the surface energy budget will become balanced ($|\Delta CRE_{long}| < 20$ W·m^{-2}; see Figure 2). The threshold was not set to 0 W·m^{-2}, as the DLW parameterization RMSE was ~20 W·m^{-2} (Wang et al., 2020).

2.6 Daily mean LST calculation

After retrieving the diurnal, all-sky LST, daily mean LST was readily calculated. To assess its accuracy, it was validated by site measurement, and the accuracy statistics were compared with three other results: one was from the official ABI LSTs, where 24 clear-sky values are available per day. The second is the daily mean from spline-interpolated 24 values in a day, and such comparison will demonstrate if the diurnal hourly LST of the proposed product is representative for daily-mean LST calculation, or whether users need to do the interpolation to obtain the daily mean by themselves. Spline interpolation is a piecewise polynomial interpolation, and it can accurately capture the variation details as we have 24 values in a diurnal cycle.

The second was the mean of two LSTs from Aqua (MYD11) at noon and midnight each day (Ouyang et al., 2012; Xing et al., 2021). This simple method has been commonly utilized in LST applications, such as temporal upscaling (Chen et al., 2017), evapotranspiration (ET) estimation (Yao et al., 2013), and permafrost monitoring (Zou et al., 2017). The last method utilizes a DTC model to interpolate the four observations from Terra + Aqua (MOD11 + MYD11) and obtain the daily mean LST. Based on a comprehensive review of DTC models (Hong et al., 2018), the GOT09 model (Göttsche and Olesen, 2009) was selected. By assuming day-to-day change of residual temperature $\delta T = 0$ and free attenuation time t_s = sunset time – 1, four unknown parameters were determined via the four observations of MOD11 + MYD11 in a day. More details about GOT09 can be found at Eq. 2 in Hong et al. (2018).

3. Results, analysis, and discussion

3.1 Configuration determination

By assuming that 18 evenly distributed sites can represent the general surface conditions over CONUS, all-sky hourly LSTs were generated using different window sizes of the dynamic model (different schemes), and then the accuracies were compared to determine the optimal configuration. Owing to computational resource limitations, only samples from different schemes in 2019 (N = 148,008 in each scheme) were used in the test.

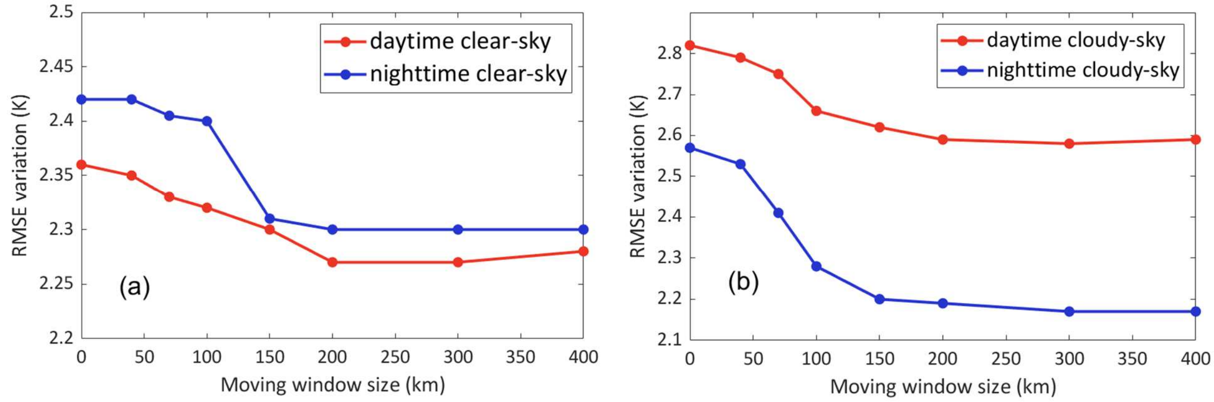

Figure 3. Overall accuracy (RMSE) of diurnal LSTs according to variable spatial window size for (a) clear- and (b) cloudy skies.

From Figure 3, it can be observed that the overall RMSE decreased when the spatial window size increased from 0 to 150 km, especially at night (Figure 3a and 3b). By including the spatial module, the nighttime cloudy-sky LST can improve the RMSE by ~0.4 K. Daytime LST showed a smaller response for window size selection. Further, it was inferred that daytime LSTs have stronger heterogeneity due to the SEB warming effect; thus, adjacent pixels at relatively farther locations may not benefit model correction, while larger spatial windows will substantially increase computation time. Accordingly, based on the site assessments over the CONUS, a 150-km window size was selected for data production.

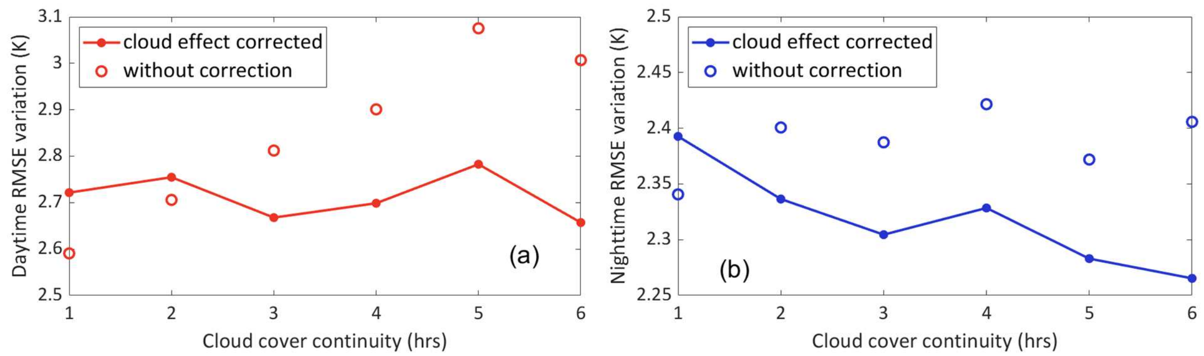

Figure 4. Overall accuracy (RMSE) during short-term cloud duration, with and without cloud effect correction, for the (a) daytime and (b) nighttime.

In order to check the necessity of cloud effect correction for short-term cloud duration cases, corresponding analysis are shown in Figure 4. It indicates that cloud effects could be neglected if the cloud coverage time was <2 h. The hypothetical clear-sky LST of 3D-KF during short-term cloud coverage (≤6 h) was tested, and the impacts of adding the estimated cloud effects were analyzed. It was revealed that cases of cloud coverage <2 h may increase uncertainty after adding the cloud effects during both the daytime and nighttime (Figure 4a and 4b). Previous research has demonstrated that the DTC interpolation model works well when the cloud duration is <4 h (Göttsche and Olesen, 2001), as the LSTs in such circumstances may not be considerably affected by clouds. Compared with the analysis in Figure 4, we determined that cloud effects were ignored if coverage was <2 h in the production. Moreover, daytime hypothetical clear-sky LST uncertainty increases with cloud duration (Figure 4a), and the cloud effect does well to address the error accumulation. Following the basic configuration tests, the all-sky hourly LSTs were derived and assessed.

3.2 Validation

The overall accuracy of the diurnal all-sky LST estimation using *in situ* measurements of the 18 field sites is shown in Figure 5. The validation results for the all-sky LSTs, and the official NOAA ABI LSTs were compared during daytime and nighttime from July 2018 to June 2021.

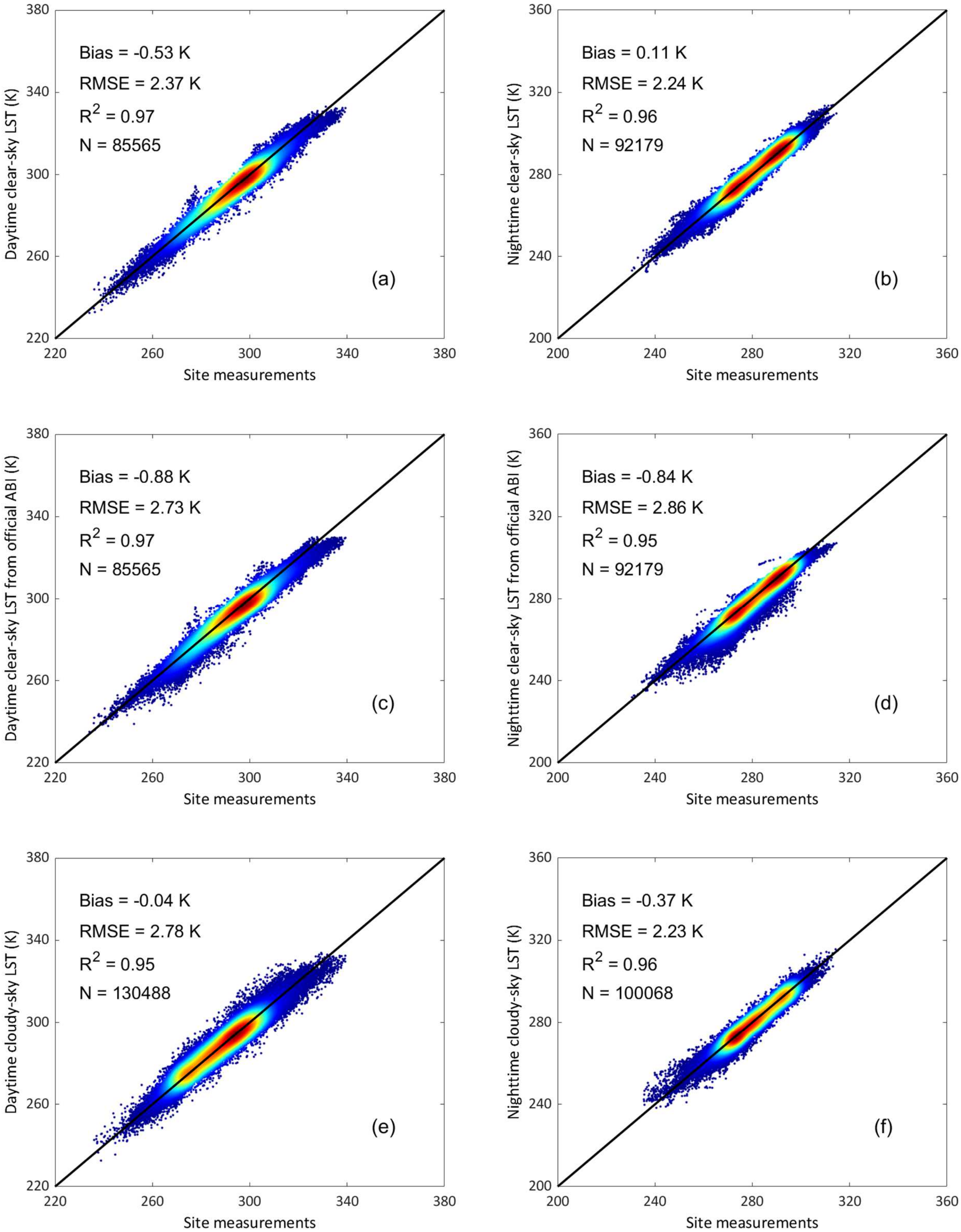
Bias = -0.53 K
RMSE = 2.37 K
R^2 = 0.97
N = 85565
(a)
Daytime clear-sky LST (K)
Site measurements
Bias = 0.11 K
RMSE = 2.24 K
R^2 = 0.96
N = 92179
(b)
Nighttime clear-sky LST (K)
Site measurements
Bias = -0.88 K
RMSE = 2.73 K
R^2 = 0.97
N = 85565
(c)
Daytime clear-sky LST from official ABI (K)
Site measurements
Bias = -0.84 K
RMSE = 2.86 K
R^2 = 0.95
N = 92179
(d)
Nighttime clear-sky LST from official ABI (K)
Site measurements
Bias = -0.04 K
RMSE = 2.78 K
R^2 = 0.95
N = 130488
(e)
Daytime cloudy-sky LST (K)
Site measurements
Bias = -0.37 K
RMSE = 2.23 K
R^2 = 0.96
N = 100068
(f)
Nighttime cloudy-sky LST (K)
Site measurements

Figure 5. Density scatterplots of LST samples from (a) present study, daytime clear-sky; (b) present study, nighttime clear-sky; (c) official ABI, daytime clear-sky; (d) official ABI, nighttime clear-sky; (e) present study, daytime cloudy-sky; and (f) present study, nighttime cloudy-sky.

The resulting product from the present study had higher accuracies than the official NOAA ABI clear-sky LST product, during both the daytime and nighttime. The daytime clear-sky samples of this study (Figure 5a) had an RMSE of 2.37 K (N = 85,565), whereas the corresponding official ABI LST product had an RMSE of 2.73 K (Figure 5c). The nighttime clear-sky samples (Figure 5b) had an RMSE of 2.24 K (N = 92,179), whereas the official ABI LST product had an RMSE of 2.86 K (Figure 5d). The latter product included some cloud-contaminated samples, particularly at night (Figure 5d), even all extracted samples of the NOAA ABI LST were marked as "good-retrieval" in the quality control flag. The contaminated pixels were distributed across Figures 5c and d, thereby creating a larger negative bias in the clear-sky validations.

Daytime cloudy-sky samples had an RMSE of 2.78 K (N = 130,488; Figure 5e), and cloudy-sky nighttime samples had an RMSE of 2.23 K (N = 100,068; Figure 5f). Based on all hourly, all-sky LST samples, the overall RMSE was 2.44 K, with a bias of -0.19 K, and an R^2 of 0.97 (N = 408,300). Likely cloud-contaminated cases identified in the data assimilation step were validated in Figure 6, while the corresponding corrected results were also included for comparison.

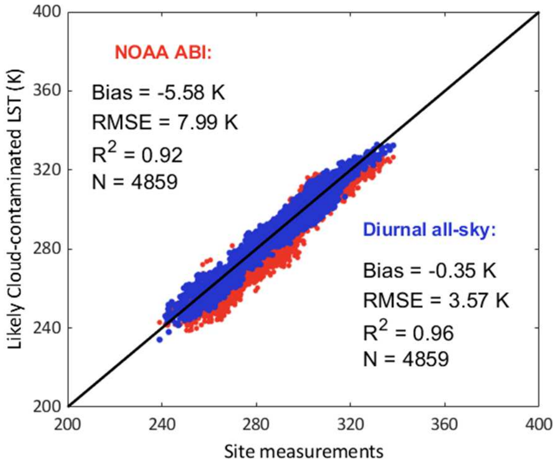

Figure 6. Scatterplot of likely cloud-contaminated samples from the official NOAA ABI and corrected results.

Figure 6 indicates that the likely cloud-contaminated pixels were recovered well. The marked official NOAA ABI LST samples had an overall RMSE of 7.99 K, largely driven by the negative bias of -5.58 K. Partially cloud-covered pixels typically have lower BT values than ground signals, resulting in abnormally cool LSTs in the images. Besides, some samples with considerably positive bias were also detected, which might be caused by the difference of the realistic surface emissivity and the climatological emissivity used in the GOES-16 LST production (Yu and Yu, 2020), and BTs with low signal-noise-ratio could be another reason. Previous studies generally ignored these disturbances that may introduce considerable uncertainties into the interpolation results. Comparatively, the accuracy of the recovered samples from this study was substantially improved (RMSE = 3.57 K). It should be noted that some clear-sky pixels might be included in Figure 6, but such misclassification won't affect the overall cloudy-sky LST estimation accuracy, owing to the high tolerance toward long cloud duration (see Section 3.3).

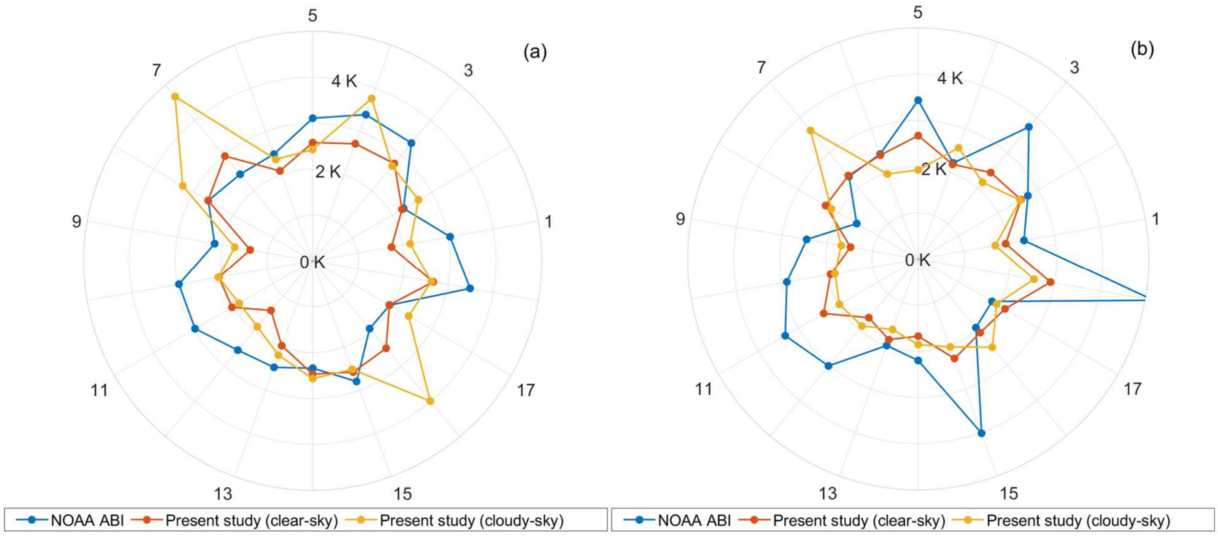

Figure 7. Comparison of the RMSE for all sites, during the (a) daytime and (b) nighttime. The radius shows RMSE values (unit: K), and exterior numbers represent the site order as indicated in Table 2.

The RMSE value comparisons for all the sites are shown in Figure 7. This suggests that the all-sky LST derived here was more accurate than the NOAA ABI across nearly all sites. NOAA ABI generally had larger RMSE patterns, especially at US-Ro5 (site 15) and US-UMB (site 18) during the nighttime (Figures 7b). Clear-sky samples of all-sky LST displayed relatively consistent accuracy levels across both the daytime and nighttime. Further, the cloudy-sky estimation accuracy was comparable to that of clear-sky LST estimates, but with a lower accuracy at TBL (site 7) and US-SRM (site 16) during the daytime. Based on further analyses, high elevations of the two sites might be the major reason that causes lower site surface representativeness (Figure 10c) and larger estimation uncertainties (Figure 14a).

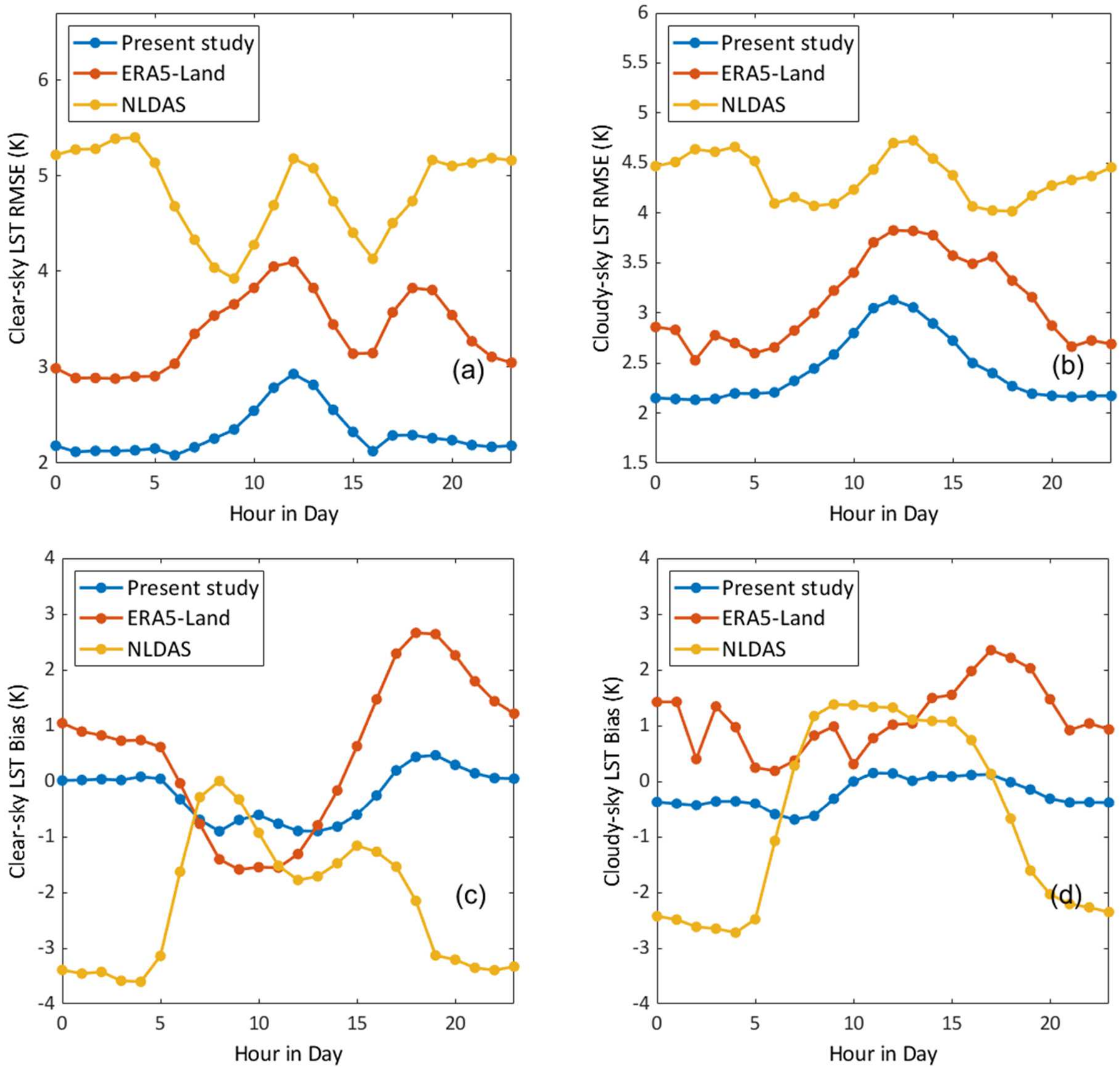

Figure 8. Comparison of the (a, b) RMSE and (c, d) Bias by hours in a day at (a, c) clear-sky and (b, d) cloudy-sky. Samples have been converted to the local time of each site.

The clear-sky and cloudy-sky LSTs at different hours in a day have been assessed, of which accuracies have also been compared with two hourly all-sky LST reanalysis datasets (Figure 8) to highlight the superiority of the proposed data. As the only currently available all-sky LST driven by satellite retrieval over CONUS and Mexico, the proposed all-sky LST performs considerably better than the simulated datasets at different hours under both clear-sky and cloudy-sky. RMSEs of the present study vary between 2.0-3.1 K at different times with bias within ± 0.7 K, and RMSEs at noon are relatively larger (Figure 8a and 8b) partly because the daytime surface is warmer that may increase the surface heterogeneity issue of site validation (Ma et al., 2021; Yoo et al., 2018). Reanalysis skin temperatures show a similar RMSE peak at noon; however, the uncertainty of NLDAS is large at night, which is attributed to the substantial cold bias (Figure 8c and 8d) (Xia et al., 2015). In comparison, ERA5-Land is more accurate than NLDAS, and even biased simulation is still an issue (Nogueira et al., 2021).

Accuracies of hourly LST reconstruction from previous algorithms and products have been summarized in Table 3. It shows the scarcity of hourly all-sky LST products, and the proposed all-sky hourly LST data perform high accuracy and advancement. It should be noted that some studies utilized an assessment method by comparing reconstructed LST with the officially retrieved LST values at artificial gaps. Such an assessment method has little surface heterogeneity issue, whereas it may not reflect the realistic cloud effect. Moreover, it may overrate the accuracy and feasibility of interpolation-based methods because artificial gaps generally have considerably smaller spatiotemporal scales than the realistic cloud, and they are essentially clear-sky LST series that have a smooth DTC curve while the cloudy-sky LST does not (Figure 10a).

Table 3. Accuracy summary of reconstructed hourly LST from previous studies.

Paper	Methodology	Outcome	Accuracy (RMSE)	Sensor	Reference data
Dumitrescu et al. (2020)	Fusion with ERA5 skin temperature	algorithm	2.46-3.35 K	MSG/SEVIRI	officially retrieved LST at artificial gaps

Liu et al. (2017b)	DTC model-based interpolation	algorithm	0.77-1.36 K	FY-2F	officially retrieved LST at artificial gaps
Wu et al. (2019)	CNN-based interpolation	algorithm	≤1 K	FY-2G and MSG/SEVIRI	officially retrieved LST at artificial gaps
Lu et al. (2011)	SEB	algorithm	5.11-5.55 K	MSG/SEVIRI	ground site measurement
Zhang et al. (2015a)	DTC model + SEB	algorithm	1.34-1.44 K	-	site measured LST at artificial gaps
Zhang et al. (2017)	SEB	algorithm	7 K	FY-2D	ground site measurement
Martins et al. (2019)	SEB	product	2.1-3.7 K	MSG/SEVIRI	ground site measurement

All-sky hourly LST provides a great opportunity for LST upscaling. The accuracy of daily mean LST generated by this study was also evaluated and compared with traditional methods in Figure 9.

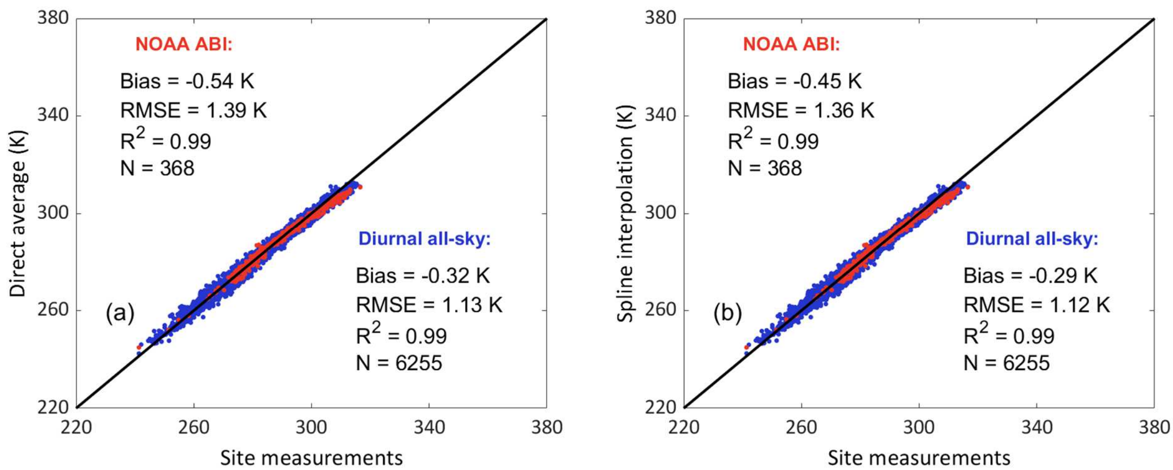

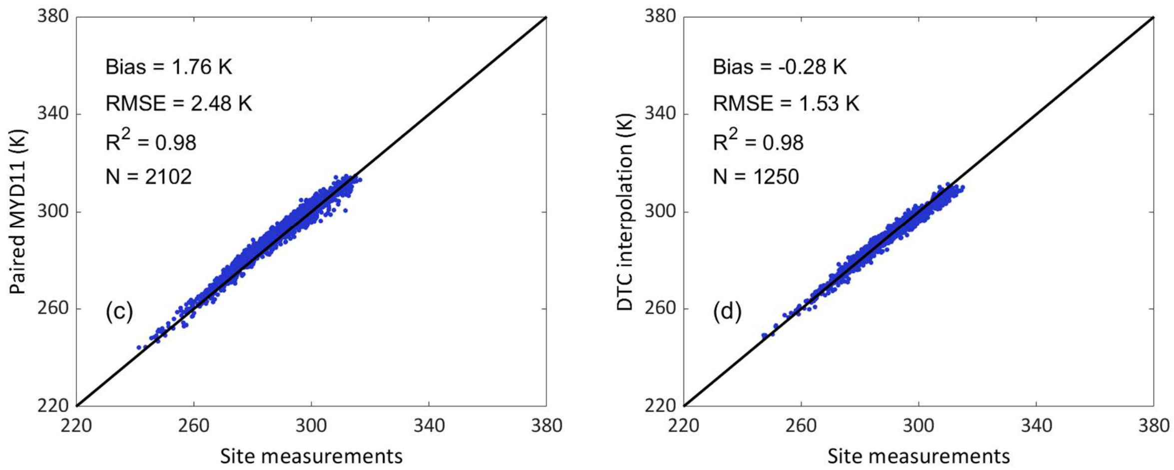

Figure 9. Scatterplots of daily mean LSTs from: (a) directly averaging 24-h values, (b) spline interpolation 24-h values, (c) paired Aqua LSTs, and (d) 4-values (Terra + Aqua) DTC interpolation.

Figure 9 illustrates the daily mean LST accuracies, as estimated from the diurnal all-sky LSTs, clear-sky NOAA ABI, two Aqua MODIS LSTs, and interpolated four Terra + Aqua MODIS observations. By directly averaging 24 hourly values, diurnal all-sky LSTs provided high accuracy estimates of the daily mean LSTs (RMSE = 1.13 K). Figure 9a shows that the daily mean of the all-sky LST is more accurate than the daily mean of the NOAA ABI for completely clear days (RMSE = 1.39 K). NOAA ABI had a relatively larger negative bias (Figure 9a), and it was thus inferred that its daily mean was influenced by cloud contamination. After spline interpolation, the daily mean LST accuracies were not improved, and the correlated bias was only slightly corrected (Figure 9b), indicating that users don't need to interpolate the 24 values for the temporal upscaling.

Daily mean LSTs from averaged MYD11 data (Figure 9c) had the largest RMSE (2.48 K). After interpolating four observations from Terra and Aqua in a day using the DTC model (Section 2.6), the resulting daily mean had an RMSE of 1.53 K (N = 1250, Figure 9d), similar to what was derived previously (Hong et al., 2018); however, the requirement of four observations per day constrained its available sample number. In comparison, diurnal, all-sky LSTs showed superiority when estimating daily mean LSTs, and thus has great potential for use in related applications (Gallego‐Elvira et al., 2016; Yao et al., 2013; Zhi-xia et al., 2011). Temporal analysis is shown in Figure 10 at hourly and daily-mean scales.

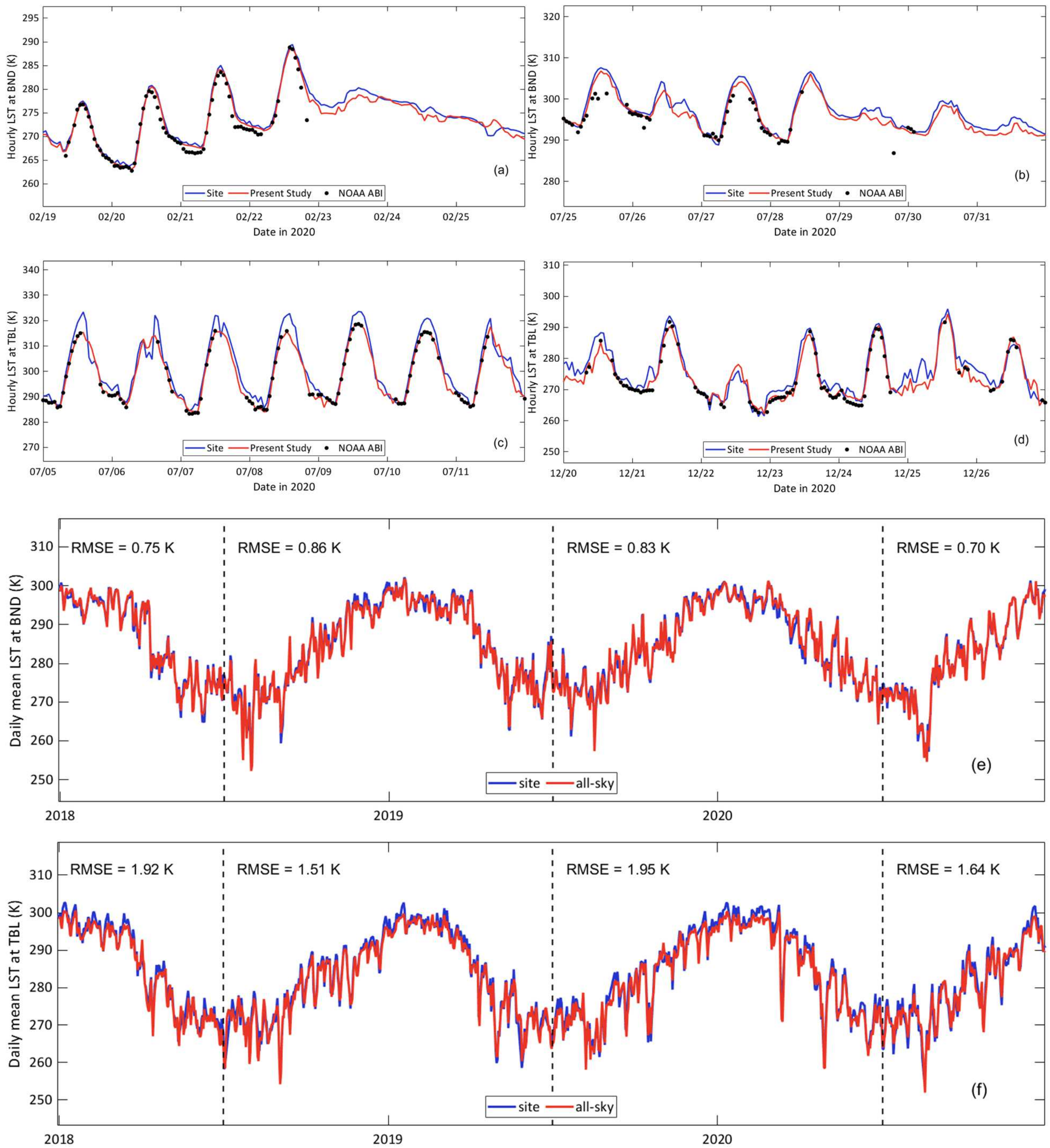

Figure 10. Time series of hourly (a-d) and daily mean (e, f) LSTs at: (a, b, and e) BND and (c, d, and f) TBL. Hourly LSTs were randomly selected from different seasons in 2020 and converted to local time.

The hourly and daily mean LST time series are shown in Figure 10 for representative sites with relatively higher and lower accuracies. Hourly LST variations in Figure 10 a-d reveal that the proposed all-sky LST well captured the realistic DTC no matter in clear days or cloudy days. Continuous cloudy days were also recovered, and the overall patterns were well matched (Figure 10a and 10b). Besides, these continuous cloudy cases also indicate the limitation of interpolation-based LST reconstruction methods as they have more various temporal patterns. Relatively larger biases were found at TBL sites, especially at noontime (Figure 10c), partially due to the higher site heterogeneity issue at noon.

Time series analysis of daily mean LSTs indicated that the all-sky LSTs were temporally contiguous, and captured not only the general patterns but also the anomalous variations; in addition, the accuracy underwent few changes over the years analyzed. The LST series at BND maintained relatively high levels of accuracy, matching well with the ground-derived measurements (Figure 10e). Comparatively, the LST series at TBL had the lowest accuracy of the seven SURFRAD sites, revealing that all-sky LSTs were underestimated, especially in the summers (Figure 10f). TBL site is at a relatively higher elevation surrounded by more complex terrain, and the relatively lower surface representativeness of TBL may partly explain the larger RMSE (Guillevic et al., 2014). The all-sky hourly LSTs were also mapped by randomly choosing three images from three seasons in 2019 for comparison with the official NOAA ABI data.

Apr. 29, 2019: 1600 (UTC)

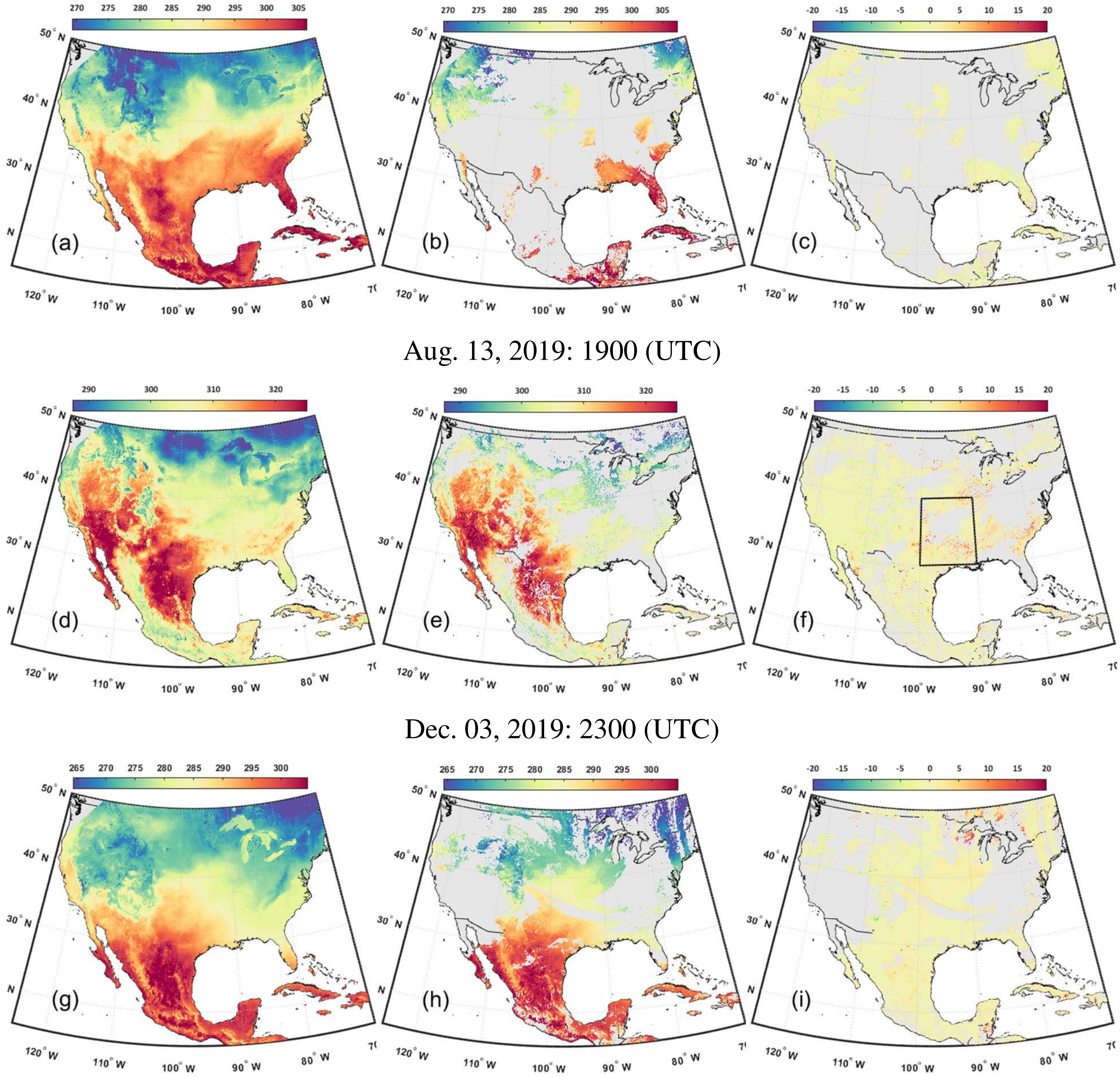

Figure 11. Hourly LSTs (unit: K) for: (a, d, g) all-sky LSTs from the present study; (b, e, h) NOAA ABI LST; and (c, f, i) the differences between the two.

Figure 11 suggests that the SEB-based method effectively recovered the all-sky diurnal LST patterns across different seasons, as well as the successful removal of cloud-contaminated pixels. The all-sky LSTs in Figure 11a, 11d, and 11g match with the NOAA ABI (Figure 11b, 11e, and 11h), and the estimated cloudy-sky LSTs are spatially continuous with the clear-sky pixels. In addition, based on the differences of all-sky and NOAA ABI LSTs, considerably positive (dark red) biases were observed along the edge of cloud patterns, as can be seen scattered in the central area of Figure 11f, and north-eastern area of Figure 11i. The partly cloud-covered pixels typically had substantially cooler BTs than the pure surface signals, resulting in negative biases reaching >20 K (Figure 6). Some mismatch appears at the west highland region partially due to the larger estimation uncertainty (Figure 14a). A detailed analysis of the LST map at the middle of the CONUS (Figure 11f) was illustrated in Figure 12.

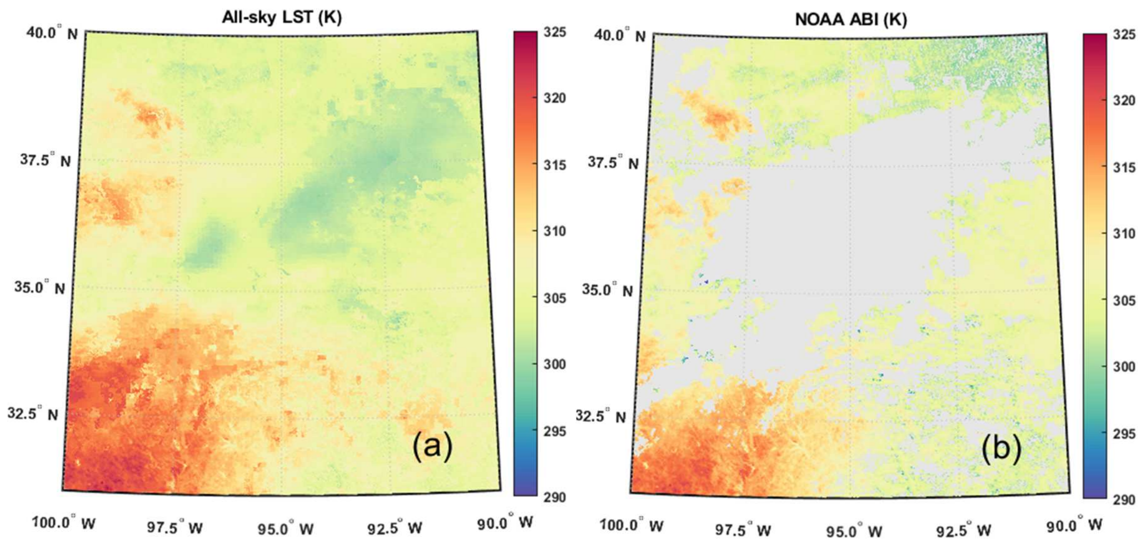

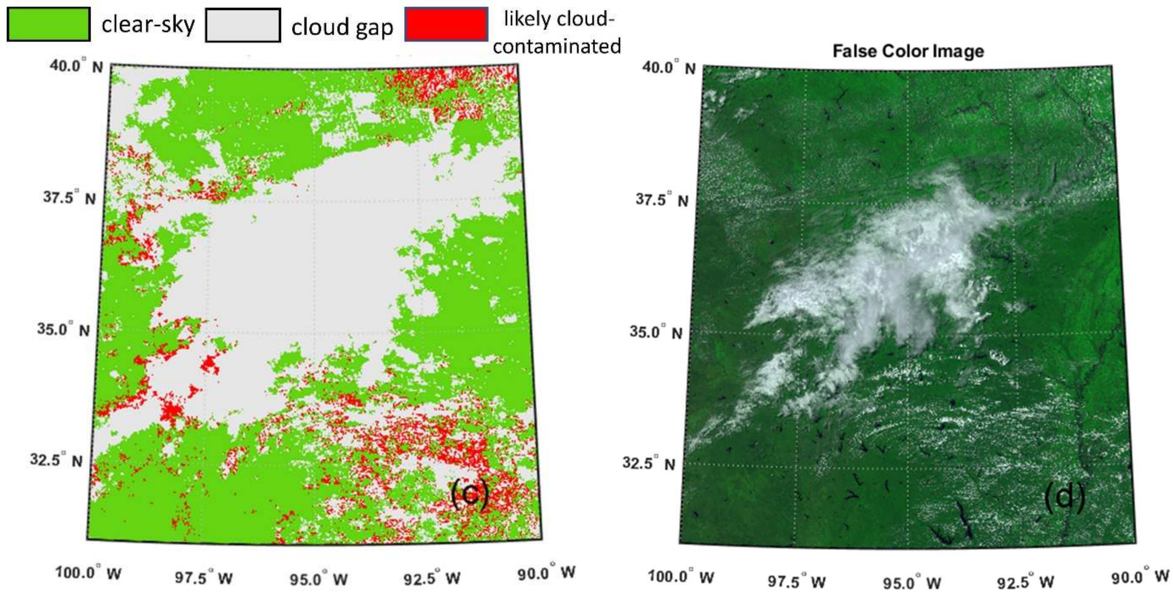

Figure 12. Regional LST maps at the marked place in Figure 11(f): (a) all-sky LST, (b) NOAA ABI, (c) pixels marked as likely cloud-contaminated, and (d) corresponding false-color image from red, near-infrared, and blue bands.

Figure 12 indicates that all-sky LST can well capture the regional variation with good spatial consistency. Compared with the clear-sky retrieval of NOAA ABI (Figure 12b), it can reflect spatial details, no matter at clear-sky (bottom left, Figure 12a) or cloudy-sky (top left, Figure 12). Besides, Figures 12a and 12d illustrate various cloud effects of different clouds: cooling effect is shown under thick cumulus in the middle, whereas cirrocumulus clouds have little cooling effect because they pass most solar energy through the atmosphere (top left, top right, and bottom right in Figure 12d). However, Figure 12a has a smooth effect over the cloud recovered regions. This is mainly due to the less spatial heterogeneity of cloudy-sky LST. In addition, 3D-KF might have filtered some spatial texture after fusing the clear-sky retrieval with simulated LSTs. Texture information from adjacent days is not easily referred to when there is a long cloud duration. Figure

12c shows that the detected cloud-contaminated pixels are mainly around the cloud pixels; besides, cloud contamination easily happens under the coverage of cirrocumulus (Figure 12d).

3.3 Impacts of cloud duration and surface elevation

Based on the assessment above, sensitivity analyses were performed to assess the robustness of the generated all-sky LST product toward extreme cloud and local conditions.

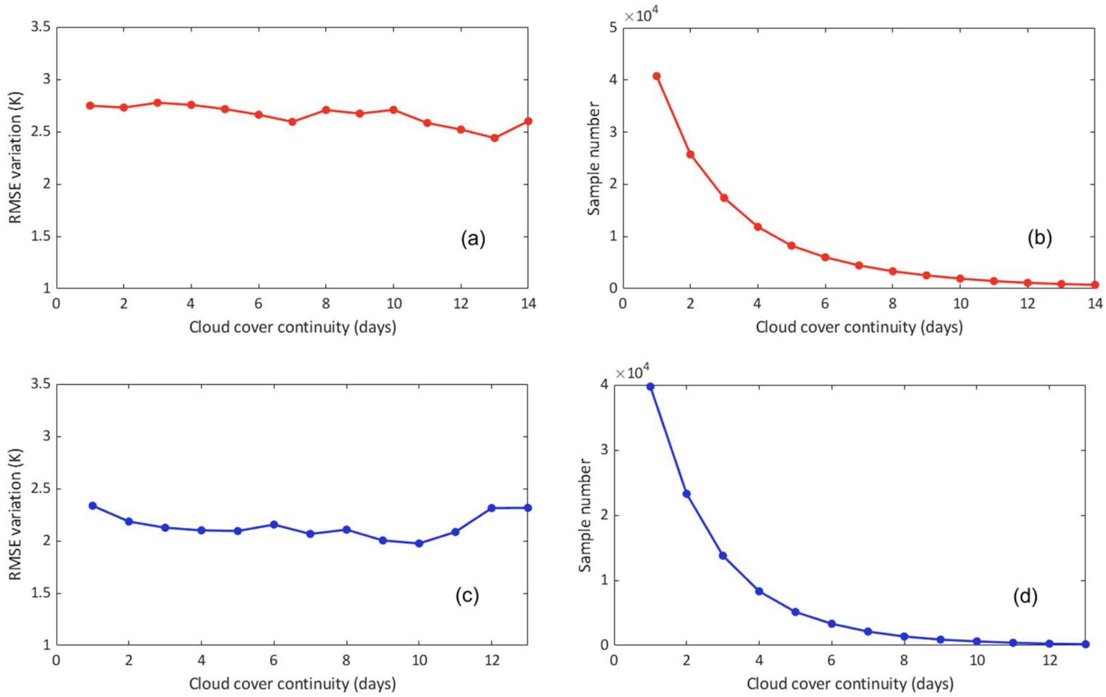

Figure 13. Overall accuracy by cloud duration, during the (a) daytime and (c) nighttime; (b, d) display the corresponding available sample numbers.

As continuous cloud duration for long periods may temporally detrimentally affect prediction accuracy until an observation is assimilated, the overall accuracy change with increasing cloud duration was quantified (Figure 13). The analyses revealed that both daytime and nighttime cloudy-sky LSTs maintained stable RMSEs. Notably, most observed cloud durations are less than 10 days, and the longer cloud duration cases that statistical numbers are less than 100 (<0.1% of the total number) were ignored (Figure 13b and 13d). Cloud duration information is included in the data quality mark, allowing users to perform quantitative analyses for specific regions or periods they plan to use.

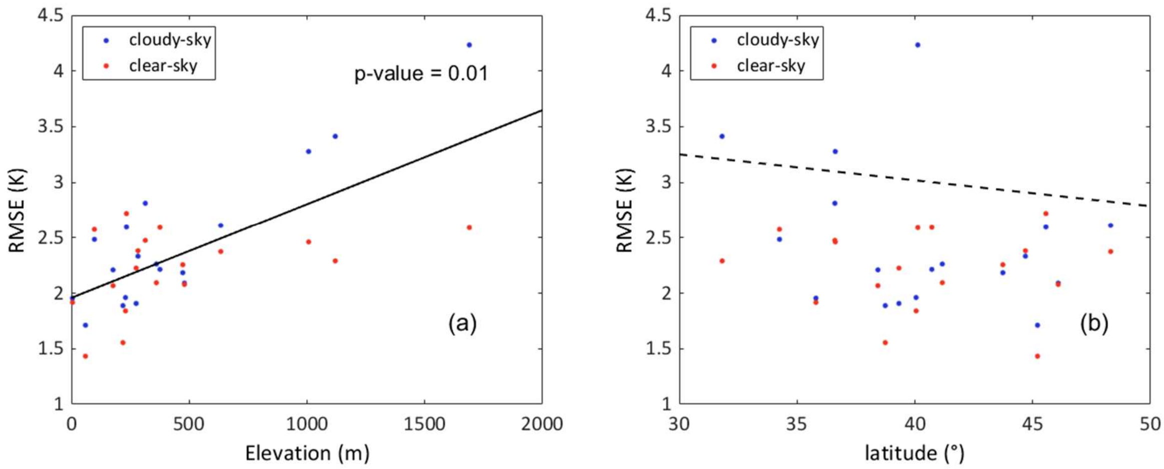

Figure 14. Accuracy of each site under clear- and cloudy-sky conditions, as a function of (a) surface elevation and (b) latitude.

The relationship between site accuracy by elevation is shown in Figure 14, revealing the correlation between accuracy and elevation. As elevation increases, as do terrain complexity and surface heterogeneity, creating difficulties for modeling simulations (Figure 14a). The impact of site latitude was also explored, as it determines the view zenith angle (VZA) of the NOAA ABI LSTs, and it has previously been found that as the VZA increases, retrieval accuracy may decrease (Yu et al., 2008). However, no such relationship was revealed here, leading to the conclusion that the all-sky LSTs produced over the CONUS all maintained relatively small VZAs (Figure 14b).

3.4 Land cover-dependent DTC climatology

DTC analyses were implemented to demonstrate that the all-sky LST product can successfully capture DTC variability. Climatological DTCs for different land cover types were characterized (Figure 15), and can potentially be used to quantify temperature feedbacks related to landcover change, and the orbit drift correction of Advanced Very High Resolution Radiometer (AVHRR) LST data (Jin and Treadon, 2003). The climatological DTCs are the multiple years' averages of DTC for different land cover types, which represent the general variation of DTC and climatological feedback by ignoring meteorological disturbance in one specific year.

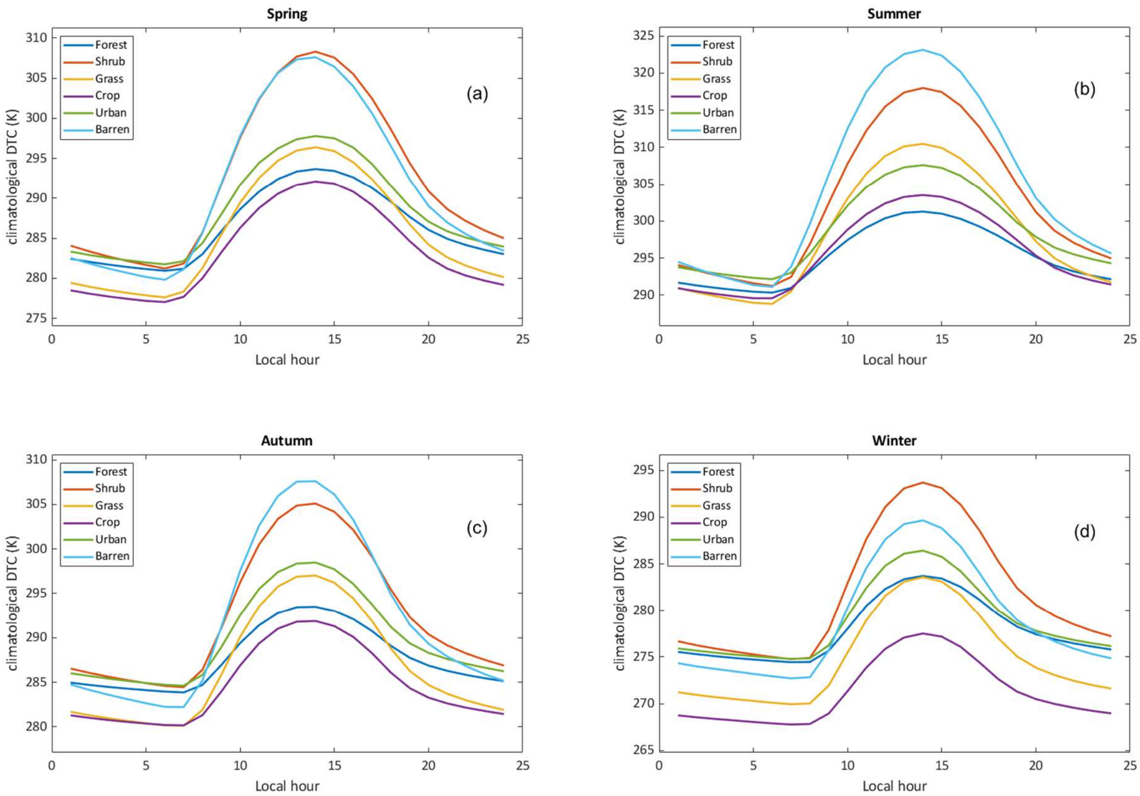

Figure 15. Climatological DTCs for different land cover types: (a) forest, (b) shrubland, (c) grassland, (d) cropland, (e) urban, and (f) barren area.

Landcover type appears to be a major factor when determining DTCs, where forests displayed the smallest diurnal temperature range (DTR), and barren areas had the largest DTR, capable of reaching ⩾30 K in summer. In addition, the temperature rise time of DTCs got delayed from summer to winter as a result of the sunrise time change based on SEB. Barren areas had the strongest response toward SEB, at both daily and seasonal scales, as local evapotranspiration is limited, and most available surface energy is partitioned into sensible and ground heat. Notably, geolocations (latitude and elevation) are also key factors influencing DTCs, and the cycle differences for various land cover types may be in part affected by them, e.g., crops are mainly at relatively high latitudes (Figure 1) and have smaller LSTs and DTCs.

4. Conclusions

By characterizing high-frequency surface thermal dynamics at medium spatial scales, GEO LSTs become invaluable for relevant studies; however, cloud coverage creates missing data and abnormal retrievals of these products, and there are few all-sky GEO LST products available to the public. Methods for GEO LST recovery have been reviewed here, revealing the following conclusions: the model fusion-based method is guaranteed gap-free, although the simulation on cloudy days is rarely corrected effectively; interpolation-based methods have lower accuracy and feasibility across larger cloud scales, nor can their results reflect realistic cloud effects on LSTs; and traditional SEB-based methods can estimate cloudy-sky LSTs, but the input requirements severely constrain its application, particularly at nighttime. In addition, few studies have discussed partial cloud contamination, an issue creating considerable uncertainty when interpolated.

Based on the SEB, a 2-km all-sky, diurnal hourly LST product over the CONUS and Mexico was created from July 2017 to June 2021. First, an original spatiotemporal dynamic model was built by ERA5, and GOES-16 ABI LST was then assimilated using 3D-KF. Finally, an innovative optimization method was proposed to estimate the diurnal cloud effects from multiple satellite radiation products, and partially cloud-contaminated pixels were also recovered.

The comprehensive assessment demonstrated the high accuracy and robustness of the all-sky LSTs using 18 sites from SURFRAD and core AmeriFlux. The RMSE values of the generated clear-sky samples for the daytime and nighttime were 2.37 and 2.24 K, respectively, which is a notable improvement over the official NOAA ABI. Further, the cloudy-sky samples during the daytime and nighttime revealed RMSE values of 2.78 and 2.23 K, respectively. Accordingly, the generated all-sky LSTs had an overall RMSE of 2.44 K, with a bias of -0.19 K and an R^2 value of 0.97 (N = 408,300), and RMSEs at different times in a day varied from 2.0 to 3.1 K. By simply averaging the diurnal hourly LSTs, the accuracy of the daily mean LST increased (RMSE = 1.13 K) compared to the daily means from paired Aqua LSTs and DTC model interpolation. Time series analysis suggested high diurnal and interannual accuracy, and mapping analyses illustrated that the recovered cloudy-sky pixels had good spatial continuity across different seasons. Cloud-contaminated pixels, shown at the cloud edges of the official clear-sky ABI images, were also recovered.

The sensitivity analyses indicated the robustness of the all-sky LSTs for different cloud and geolocation conditions. The proposed data have a high tolerance toward long cloud duration. Moreover, higher elevations may decrease the estimation accuracy of cloudy times, although the VZA had little impact on product accuracy over the study area observed. DTC analysis showed climatologically seasonal variations across different land cover types, demonstrating that the all-sky hourly LST product was superior for characterizing DTC variability, and has great potential for future research use.

Ground validation and DTC analyses exhibited the readiness and robustness of this approach for further scientific application. The proposed method here is sensor-independent, and can potentially be implemented for other similar GEO LST products. Based on the results of the present study, all-sky diurnal air temperature and heat fluxes will be the focus of future research.

Acknowledgments

The diurnal all-sky ABI LST product is available at the University of Maryland (http://glass.umd.edu/allsky_ABI_LST/). The authors gratefully acknowledge the National Center for Atmospheric Research (NCAR) Computational & Information System Lab (CISL) for providing the computational resources for data production. We also would like to thank the NOAA ABI LST group (https://www.avl.class.noaa.gov/), NASA MODIS science team (https://earthdata.nasa.gov/), ECMWF ERA5 (https://www.ecmwf.int/), CERES (https://ceres.larc.nasa.gov/), and GLASS project (http://glass.umd.edu/) for providing the datasets. Ground measurements were collected from the SURFRAD (https://gml.noaa.gov/grad/surfrad/) and AmeriFlux (https://ameriflux.lbl.gov/) networks. We sincerely acknowledge three anonymous reviewers for their constructive comments and Peng Yu for his invaluable insight regarding product assessment.

Author contributions

S. Liang conceived the scope of this study; A. Jia processed the data; A. Jia, S. Liang, and D. Wang interpreted the results; A. Jia wrote the manuscript. All authors contributed to the revision of the article.

Declaration of Competing Interest

The authors declare that they have no known competing financial interests or personal relationships that could have influenced the work reported in this paper.

References

Aires, F., Prigent, C., & Rossow, W. (2004). Temporal interpolation of global surface skin temperature diurnal cycle over land under clear and cloudy conditions. *Journal of Geophysical Research: Atmospheres, 109*

AmeriFlux (2021). What are the AmeriFlux Core Sites? In. https://ameriflux.lbl.gov/sites/ameriflux-core-sites/ (access date: July 30, 2021)

Anderson, M.C., Norman, J.M., Mecikalski, J.R., Otkin, J.A., & Kustas, W.P. (2007). A climatological study of evapotranspiration and moisture stress across the continental United States based on thermal remote sensing: 2. Surface moisture climatology. *Journal of Geophysical Research: Atmospheres, 112*

Arboleda, A., Ghilain, N., & Gellens-Meulenberghs, F. (2017). Continuous monitoring of evapotranspiration (ET) overview of LSA-SAF evapotranspiration products. *Remote Sensing for Agriculture, Ecosystems, and Hydrology Xix, 10421*

Augustine, J.A., DeLuisi, J.J., & Long, C.N. (2000). SURFRAD - A national surface radiation budget network for atmospheric research. *Bulletin of the American Meteorological Society, 81*, 2341-2357

Beckers, J.M., Barth, A., Tomazic, I., & Alvera-Azcarate, A. (2014). A method to generate fully multi-scale optimal interpolation by combining efficient single process analyses, illustrated by a DINEOF analysis spiced with a local optimal interpolation. *Ocean Science, 10*, 845-862

Blackett, M., Wooster, M.J., & Malamud, B.D. (2011). Exploring land surface temperature earthquake precursors: A focus on the Gujarat (India) earthquake of 2001. *Geophysical Research Letters, 38*

Chen, J.M., & Liu, J. (2020). Evolution of evapotranspiration models using thermal and shortwave remote sensing data. *Remote Sensing of Environment, 237*, 111594

Chen, X., Su, Z., Ma, Y., Cleverly, J., & Liddell, M. (2017). An accurate estimate of monthly mean land surface temperatures from MODIS clear-sky retrievals. *Journal of Hydrometeorology, 18*, 2827-2847

Cheng, J., Yang, F., & Guo, Y. (2019). A Comparative Study of Bulk Parameterization Schemes for Estimating Cloudy-Sky Surface Downward Longwave Radiation. *Remote Sensing, 11*, 528

Chuvieco, E., Cocero, D., Riano, D., Martin, P., Martınez-Vega, J., De La Riva, J., & Pérez, F. (2004). Combining NDVI and surface temperature for the estimation of live fuel moisture content in forest fire danger rating. *Remote Sensing of Environment, 92*, 322-331

Danielson, J.J., & Gesch, D.B. (2011). *Global multi-resolution terrain elevation data 2010 (GMTED2010)*. US Department of the Interior, US Geological Survey

Dash, P., Göttsche, F.-M., Olesen, F.-S., & Fischer, H. (2002). Land surface temperature and emissivity estimation from passive sensor data: Theory and practice-current trends. *International Journal of remote sensing, 23*, 2563-2594

Delmotte, V., Zhai, P., Pörtner, H.-O., Roberts, D., Skea, J., Shukla, P.R., Pirani, A., Moufouma-Okia, W., Péan, C., & Pidcock, R. (2018). Global warming of 1.5 C. *An IPCC Special Report on the impacts of global warming, 1*, 1

Delmotte, V., Zhai;, P., & A. Pirani, S.L.C., C. Péan, S. Berger, N. Caud, Y. Chen, L. Goldfarb, M. I. Gomis, M. Huang, K. Leitzell, E. Lonnoy, J. B. R. Matthews, T. K. Maycock, T. Waterfield, O. Yelekçi, R. Yu and B. Zhou (eds.)]. (2021). IPCC, 2021: Summary for Policymakers. In: Climate Change 2021: The Physical Science Basis. Contribution of Working Group I to the Sixth Assessment Report of the Intergovernmental Panel on Climate Change. In. Cambridge University Press.In Press.

Duan, S.-B., Li, Z.-L., Tang, B.-H., Wu, H., Tang, R., Bi, Y., & Zhou, G. (2014). Estimation of diurnal cycle of land surface temperature at high temporal and spatial resolution from clear-sky MODIS data. *Remote Sensing, 6*, 3247-3262

Duan, S.-B., Li, Z.-L., Wang, N., Wu, H., & Tang, B.-H. (2012). Evaluation of six land-surface diurnal temperature cycle models using clear-sky in situ and satellite data. *Remote Sensing of Environment, 124*, 15-25

Duan, S.B., Li, Z.L., & Leng, P. (2017). A framework for the retrieval of all-weather land surface temperature at a high spatial resolution from polar-orbiting thermal infrared and passive microwave data. *Remote Sensing of Environment, 195*, 107-117

Dumitrescu, A., Brabec, M., & Cheval, S. (2020). Statistical Gap-Filling of SEVIRI Land Surface Temperature. *Remote Sensing, 12*, 1423

Ermida, S.L., Trigo, I.F., DaCamara, C.C., Jiménez, C., & Prigent, C. (2019). Quantifying the clear‐sky bias of satellite land surface temperature using microwave‐based estimates. *Journal of Geophysical Research: Atmospheres, 124*, 844-857

Fablet, R., Viet, P.H., & Lguensat, R. (2017). Data-driven Models for the Spatio-Temporal Interpolation of satellite-derived SST Fields. *IEEE Transactions on Computational Imaging, 3*, 647-657

Fensholt, R., Anyamba, A., Huber, S., Proud, S.R., Tucker, C.J., Small, J., Pak, E., Rasmussen, M.O., Sandholt, I., & Shisanya, C. (2011). Analysing the advantages of high temporal resolution geostationary MSG SEVIRI data compared to Polar Operational Environmental Satellite data for land surface monitoring in Africa. *International journal of applied earth observation and geoinformation, 13*, 721-729

Freitas, S.C., Trigo, I.F., Bioucas-Dias, J.M., & Gottsche, F.-M. (2009). Quantifying the uncertainty of land surface temperature retrievals from SEVIRI/Meteosat. *IEEE Transactions on Geoscience and Remote Sensing, 48*, 523-534

Freitas, S.C., Trigo, I.F., Macedo, J., Barroso, C., Silva, R., & Perdigão, R. (2013). Land surface temperature from multiple geostationary satellites. *International Journal of remote sensing, 34*, 3051-3068

Fu, P., Xie, Y., Weng, Q., Myint, S., Meacham-Hensold, K., & Bernacchi, C. (2019). A physical model-based method for retrieving urban land surface temperatures under cloudy conditions. *Remote Sensing of Environment, 230*, 111191

Fu, Q., Liou, K., Cribb, M., Charlock, T., & Grossman, A. (1997). Multiple scattering parameterization in thermal infrared radiative transfer. *Journal of the Atmospheric Sciences, 54*, 2799-2812

Gallego‐Elvira, B., Taylor, C.M., Harris, P.P., Ghent, D., Veal, K.L., & Folwell, S.S. (2016). Global observational diagnosis of soil moisture control on the land surface energy balance. *Geophysical Research Letters, 43*, 2623-2631

Ghafarian, H.R., Menenti, M., Jia, L., & den Ouden, H. (2012). Reconstruction of cloud-free time series satellite observations of land surface temperature. *EARSel eProc, 11*, 123-131

Göttsche, F.-M., & Olesen, F.-S. (2009). Modelling the effect of optical thickness on diurnal cycles of land surface temperature. *Remote Sensing of Environment, 113*, 2306-2316

Göttsche, F.-M., & Olesen, F.S. (2001). Modelling of diurnal cycles of brightness temperature extracted from METEOSAT data. *Remote Sensing of Environment, 76*, 337-348

Gottsche, F.M., & Olesen, F.S. (2009). Modelling the effect of optical thickness on diurnal cycles of land surface temperature. *Remote Sensing of Environment, 113*, 2306-2316

Guillevic, P.C., Biard, J.C., Hulley, G.C., Privette, J.L., Hook, S.J., Olioso, A., Göttsche, F.M., Radocinski, R., Román, M.O., & Yu, Y. (2014). Validation of Land Surface Temperature products derived from the Visible Infrared Imaging Radiometer Suite (VIIRS) using ground-based and heritage satellite measurements. *Remote Sensing of Environment, 154*, 19-37

He, T., Liang, S., & Song, D.X. (2014). Analysis of global land surface albedo climatology and spatial‐temporal variation during 1981–2010 from multiple satellite products. *Journal of Geophysical Research: Atmospheres, 119*, 10,281-210,298

Heidinger, A., Pavolonis, M., Holz, R., Baum, B.A., & Berthier, S. (2010). Using CALIPSO to explore the sensitivity to cirrus height in the infrared observations from NPOESS/VIIRS and GOES‐R/ABI. *Journal of Geophysical Research: Atmospheres, 115*

Heidinger, A.K., Pavolonis, M.J., Calvert, C., Hoffman, J., Nebuda, S., Straka III, W., Walther, A., & Wanzong, S. (2020). ABI cloud products from the GOES-R series. *The GOES-R Series* (pp. 43-62): Elsevier

Hersbach, H., Bell, B., Berrisford, P., Hirahara, S., Horanyi, A., Munoz-Sabater, J., Nicolas, J., Peubey, C., Radu, R., Schepers, D., Simmons, A., Soci, C., Abdalla, S., Abellan, X., Balsamo, G., Bechtold, P., Biavati, G., Bidlot, J., Bonavita, M., De Chiara, G., Dahlgren, P., Dee, D., Diamantakis, M., Dragani, R., Flemming, J., Forbes, R., Fuentes, M., Geer, A., Haimberger, L., Healy, S., Hogan, R.J., Holm, E., Janiskova, M., Keeley, S., Laloyaux, P., Lopez, P., Lupu, C., Radnoti, G., de Rosnay, P., Rozum, I., Vamborg, F., Villaume, S., & Thepaut, J.N. (2020). The ERA5 global reanalysis. *Quarterly Journal of the royal meteorological society, 146*, 1999-2049

Holmes, T., Crow, W., & Hain, C. (2013). Spatial patterns in timing of the diurnal temperature cycle. *Hydrology and Earth System Sciences, 17*, 3695-3706

Holmes, T., Crow, W., Hain, C., Anderson, M., & Kustas, W. (2015). Diurnal temperature cycle as observed by thermal infrared and microwave radiometers. *Remote Sensing of Environment, 158*, 110-125

Hong, F., Zhan, W., Göttsche, F.-M., Lai, J., Liu, Z., Hu, L., Fu, P., Huang, F., Li, J., & Li, H. (2021). A simple yet robust framework to estimate accurate daily mean land surface temperature from thermal observations of tandem polar orbiters. *Remote Sensing of Environment, 264*, 112612

Hong, F.L., Zhan, W.F., Gottsche, F.M., Liu, Z.H., Zhou, J., Huang, F., Lai, J.M., & Li, M.C. (2018). Comprehensive assessment of four-parameter diurnal land surface temperature cycle models under clear-sky. *ISPRS Journal of Photogrammetry and Remote Sensing, 142*, 190-204

Hrisko, J., Ramamurthy, P., Yu, Y., Yu, P., & Melecio-Vázquez, D. (2020). Urban air temperature model using GOES-16 LST and a diurnal regressive neural network algorithm. *Remote Sensing of Environment, 237*, 111495

Huang, F., Zhan, W., Duan, S.-B., Ju, W., & Quan, J. (2014). A generic framework for modeling diurnal land surface temperatures with remotely sensed thermal observations under clear sky. *Remote Sensing of Environment, 150*, 140-151

Ignatov, A., & Gutman, G. (1999). Monthly mean diurnal cycles in surface temperatures over land for global climate studies. *Journal of Climate, 12*, 1900-1910

Imhoff, M.L., Zhang, P., Wolfe, R.E., & Bounoua, L. (2010). Remote sensing of the urban heat island effect across biomes in the continental USA. *Remote Sensing of Environment, 114*, 504-513

Inamdar, A.K., & French, A. (2009). Disaggregation of GOES land surface temperatures using surface emissivity. *Geophysical Research Letters, 36*

Inamdar, A.K., French, A., Hook, S., Vaughan, G., & Luckett, W. (2008). Land surface temperature retrieval at high spatial and temporal resolutions over the southwestern United States. *Journal of Geophysical Research: Atmospheres, 113*

Jia, A., Liang, S., Jiang, B., Zhang, X., & Wang, G. (2018). Comprehensive assessment of global surface net radiation products and uncertainty analysis. *Journal of Geophysical Research: Atmospheres, 123*, 1970-1989

Jia, A., Liang, S., Wang, D., Jiang, B., & Zhang, X. (2020). Air pollution slows down surface warming over the Tibetan Plateau. *Atmospheric Chemistry and Physics, 20*, 881-899

Jia, A., Ma, H., Liang, S., & Wang, D. (2021). Cloudy-sky land surface temperature from VIIRS and MODIS satellite data using a surface energy balance-based method. *Remote Sensing of Environment, 263*, 112566

Jiang, B., Liang, S., Jia, A., Xu, J., Zhang, X., Xiao, Z., Zhao, X., Jia, K., & Yao, Y. (2018). Validation of the Surface Daytime Net Radiation Product From Version 4.0 GLASS Product Suite. *IEEE Geoscience and Remote Sensing Letters*

Jiang, G.-M., Li, Z.-L., & Nerry, F. (2006). Land surface emissivity retrieval from combined mid-infrared and thermal infrared data of MSG-SEVIRI. *Remote Sensing of Environment, 105*, 326-340

Jiang, Y., Fu, P., & Weng, Q. (2015). Downscaling GOES land surface temperature for assessing heat wave health risks. *IEEE Geoscience and Remote Sensing Letters, 12*, 1605-1609

Jin, M. (2000). Interpolation of surface radiative temperature measured from polar orbiting satellites to a diurnal cycle: 2. Cloudy - pixel treatment. *Journal of Geophysical Research: Atmospheres, 105*, 4061-4076

Jin, M. (2004). Analysis of land skin temperature using AVHRR observations. *Bulletin of the American Meteorological Society, 85*, 587-600

Jin, M., & Dickinson, R.E. (2000). A generalized algorithm for retrieving cloudy sky skin temperature from satellite thermal infrared radiances. *Journal of Geophysical Research: Atmospheres, 105*, 27037-27047

Jin, M., & Treadon, R. (2003). Correcting the orbit drift effect on AVHRR land surface skin temperature measurements. *International Journal of remote sensing, 24*, 4543-4558

Karnieli, A., Agam, N., Pinker, R.T., Anderson, M., Imhoff, M.L., Gutman, G.G., Panov, N., & Goldberg, A. (2010). Use of NDVI and land surface temperature for drought assessment: Merits and limitations. *Journal of Climate, 23*, 618-633

Kato, S., Rose, F.G., Rutan, D.A., Thorsen, T.J., Loeb, N.G., Doelling, D.R., Huang, X., Smith, W.L., Su, W., & Ham, S.-H. (2018). Surface Irradiances of Edition 4.0 Clouds and the Earth's Radiant Energy System (CERES) Energy Balanced and Filled (EBAF) Data Product. *Journal of Climate, 31*, 4501-4527

Kidd, C., Kniveton, D.R., Todd, M.C., & Bellerby, T.J. (2003). Satellite rainfall estimation using combined passive microwave and infrared algorithms. *Journal of Hydrometeorology, 4*, 1088-1104

Laszlo, I., Liu, H., Kim, H.-Y., & Pinker, R.T. (2020). Shortwave Radiation from ABI on the GOES-R Series. *The GOES-R Series* (pp. 179-191): Elsevier

Letu, H., Nakajima, T.Y., Wang, T., Shang, H., Ma, R., Yang, K., Baran, A.J., Riedi, J., Ishimoto, H., & Yoshida, M. (2021). A new benchmark for surface radiation products over the East Asia-Pacific region retrieved from the Himawari-8/AHI next-generation geostationary satellite. *Bulletin of the American Meteorological Society*, 1-40

Li, B., Liang, S., Liu, X., Ma, H., Chen, Y., Liang, T., & He, T. (2021). Estimation of all-sky 1 km land surface temperature over the conterminous United States. *Remote Sensing of Environment, 266*, 112707

Li, Z.-L., Tang, B.-H., Wu, H., Ren, H., Yan, G., Wan, Z., Trigo, I.F., & Sobrino, J.A. (2013). Satellite-derived land surface temperature: Current status and perspectives. *Remote Sensing of Environment, 131*, 14-37

Liang, S., Cheng, J., Jia, K., Jiang, B., Liu, Q., Xiao, Z., Yao, Y., Yuan, W., Zhang, X., & Zhao, X. (2021). The global Land surface satellite (GLASS) product suite. *Bulletin of the American Meteorological Society, 102*, E323-E337

Liang, S., Wang, K.C., Zhang, X.T., & Wild, M. (2010). Review on Estimation of Land Surface Radiation and Energy Budgets From Ground Measurement, Remote Sensing and Model Simulations. *IEEE Journal of Selected Topics in Applied Earth Observations and Remote Sensing, 3*, 225-240

Liu, Z., Wu, P., Wu, Y., Shen, H., & Zeng, C. (2017a). Robust reconstruction of missing data in Feng Yun geostationary satellite land surface temperature products (Chinese). *Journal of Remote Sensing, 21*, 40-51

Liu, Z.H., Wu, P.H., Duan, S.B., Zhan, W.F., Ma, X.S., & Wu, Y.L. (2017b). Spatiotemporal Reconstruction of Land Surface Temperature Derived From FengYun Geostationary Satellite

Data. *IEEE Journal of Selected Topics in Applied Earth Observations and Remote Sensing, 10*, 4531-4543

Long, D., Yan, L., Bai, L., Zhang, C., Li, X., Lei, H., Yang, H., Tian, F., Zeng, C., Meng, X., & Shi, C. (2020). Generation of MODIS-like land surface temperatures under all-weather conditions based on a data fusion approach. *Remote Sensing of Environment, 246*, 111863

Lu, L., Venus, V., Skidmore, A., Wang, T., & Luo, G. (2011). Estimating land-surface temperature under clouds using MSG/SEVIRI observations. *International journal of applied earth observation and geoinformation, 13*, 265-276

Ma, J., Zhou, J., Göttsche, F.-M., Liang, S., Wang, S., & Li, M. (2020). A global long-term (1981–2000) land surface temperature product for NOAA AVHRR. *Earth System Science Data, 12*, 3247-3268

Ma, J., Zhou, J., Liu, S., Göttsche, F.-M., Zhang, X., Wang, S., & Li, M. (2021). Continuous evaluation of the spatial representativeness of land surface temperature validation sites. *Remote Sensing of Environment, 265*, 112669

Martins, J.P.A., Trigo, I.F., Ghilain, N., Jimenez, C., Gottsche, F.M., Ermida, S.L., Olesen, F.S., Gellens-Meulenberghs, F., & Arboleda, A. (2019). An All-Weather Land Surface Temperature Product Based on MSG/SEVIRI Observations. *Remote Sensing, 11*

Marullo, S., Santoleri, R., Banzon, V., Evans, R.H., & Guarracino, M. (2010). A diurnal-cycle resolving sea surface temperature product for the tropical Atlantic. *Journal of Geophysical Research-Oceans, 115*

Marullo, S., Santoleri, R., Ciani, D., Le Borgne, P., Pere, S., Pinardi, N., Tonani, M., & Nardone, G. (2014). Combining model and geostationary satellite data to reconstruct hourly SST field over the Mediterranean Sea. *Remote Sensing of Environment, 146*, 11-23

Mo, Y., Xu, Y., Chen, H., & Zhu, S. (2021). A Review of Reconstructing Remotely Sensed Land Surface Temperature under Cloudy Conditions. *Remote Sensing, 13*, 2838

Murphy, S.C., Nazzaro, L.J., Simkins, J., Oliver, M.J., Kohut, J., Crowley, M., & Miles, T.N. (2021). Persistent upwelling in the Mid-Atlantic Bight detected using gap-filled, high-resolution satellite SST. *Remote Sensing of Environment, 262*, 112487

Nardelli, B.B., Pisano, A., Tronconi, C., & Santoleri, R. (2015). Evaluation of different covariance models for the operational interpolation of high resolution satellite Sea Surface Temperature data over the Mediterranean Sea. *Remote Sensing of Environment, 164*, 334-343

Neteler, M. (2010). Estimating daily land surface temperatures in mountainous environments by reconstructed MODIS LST data. *Remote Sensing, 2*, 333-351

Neteler, M., Roiz, D., Rocchini, D., Castellani, C., & Rizzoli, A. (2011). Terra and Aqua satellites track tiger mosquito invasion: modelling the potential distribution of Aedes albopictus in north-eastern Italy. *International Journal of Health Geographics, 10*, 1-14

Nogueira, M., Boussetta, S., Balsamo, G., Albergel, C., Trigo, I.F., Johannsen, F., Miralles, D.G., & Dutra, E. (2021). Upgrading Land ‐ Cover and Vegetation Seasonality in the ECMWF Coupled System: Verification With FLUXNET Sites, METEOSAT Satellite Land Surface Temperatures, and ERA5 Atmospheric Reanalysis. *Journal of Geophysical Research: Atmospheres, 126*, e2020JD034163

Orth, R., Dutra, E., Trigo, I.F., & Balsamo, G. (2017). Advancing land surface model development with satellite-based Earth observations. *Hydrology and Earth System Sciences, 21*, 2483-2495

Ouyang, B., Che, T., DAI, L.-y., & WANG, Z.-y. (2012). Estimating Mean Daily Surface Temperature over the Tibetan Plateau Based on MODIS LST Products [J]. *Journal of Glaciology and Geocryology, 2*, 296-303

Parton, W.J., & Logan, J.A. (1981). A model for diurnal variation in soil and air temperature. *Agricultural Meteorology, 23*, 205-216

Piles, M., Petropoulos, G.P., Sánchez, N., González-Zamora, Á., & Ireland, G. (2016). Towards improved spatio-temporal resolution soil moisture retrievals from the synergy of SMOS and MSG SEVIRI spaceborne observations. *Remote Sensing of Environment, 180*, 403-417

Pinker, R.T., Tarpley, J.D., Laszlo, I., Mitchell, K.E., Houser, P.R., Wood, E.F., Schaake, J.C., Robock, A., Lohmann, D., & Cosgrove, B.A. (2003). Surface radiation budgets in support of the GEWEX Continental - Scale International Project (GCIP) and the GEWEX Americas Prediction Project (GAPP), including the North American Land Data Assimilation System (NLDAS) project. *Journal of Geophysical Research: Atmospheres, 108*

Quan, J., Chen, Y., Zhan, W., Wang, J., Voogt, J., & Li, J. (2014). A hybrid method combining neighborhood information from satellite data with modeled diurnal temperature cycles over consecutive days. *Remote Sensing of Environment, 155*, 257-274

Quan, J., Zhan, W., Ma, T., Du, Y., Guo, Z., & Qin, B. (2018). An integrated model for generating hourly Landsat-like land surface temperatures over heterogeneous landscapes. *Remote Sensing of Environment, 206*, 403-423

Rao, Y., Liang, S., Wang, D., Yu, Y., Song, Z., Zhou, Y., Shen, M., & Xu, B. (2019). Estimating daily average surface air temperature using satellite land surface temperature and top-of-atmosphere radiation products over the Tibetan Plateau. *Remote Sensing of Environment, 234*, 111462

Schaaf, C.B., Gao, F., Strahler, A.H., Lucht, W., Li, X., Tsang, T., Strugnell, N.C., Zhang, X., Jin, Y., & Muller, J.-P. (2002). First operational BRDF, albedo nadir reflectance products from MODIS. *Remote Sensing of Environment, 83*, 135-148

Schädlich, S., Göttsche, F., & Olesen, F.-S. (2001). Influence of land surface parameters and atmosphere on METEOSAT brightness temperatures and generation of land surface temperature maps by temporally and spatially interpolating atmospheric correction. *Remote Sensing of Environment, 75*, 39-46

Stisen, S., Sandholt, I., Nørgaard, A., Fensholt, R., & Jensen, K.H. (2008). Combining the triangle method with thermal inertia to estimate regional evapotranspiration—Applied to MSG-SEVIRI data in the Senegal River basin. *Remote Sensing of Environment, 112*, 1242-1255

Sulla-Menashe, D., & Friedl, M.A. (2018). User guide to collection 6 MODIS land cover (MCD12Q1 and MCD12C1) product. *USGS: Reston, VA, USA*, 1-18

Tang, B., Bi, Y., Li, Z.-L., & Xia, J. (2008). Generalized split-window algorithm for estimate of land surface temperature from Chinese geostationary FengYun meteorological satellite (FY-2C) data. *Sensors, 8*, 933-951

Udahemuka, G., Van Den Bergh, F., Van Wyk, B., & Van Wyk, M. (2008). Robust fitting of diurnal brightness temperature cycles: pattern recognition special edition*, 40*, 31-36

Ushio, T., Sasashige, K., Kubota, T., Shige, S., Okamoto, K.i., Aonashi, K., Inoue, T., Takahashi, N., Iguchi, T., & Kachi, M. (2009). A Kalman filter approach to the Global Satellite Mapping of Precipitation (GSMaP) from combined passive microwave and infrared radiometric data. *Journal of the Meteorological Society of Japan. Ser. II, 87*, 137-151

Van de Griend, A., Camillo, P., & Gurney, R. (1985). Discrimination of soil physical parameters, thermal inertia, and soil moisture from diurnal surface temperature fluctuations. *Water Resources Research, 21*, 997-1009

Van den Bergh, F., Van Wyk, M., Van Wyk, B., & Udahemuka, G. (2007). A comparison of data-driven and model-driven approaches to brightness temperature diurnal cycle interpolation. *SAIEE Africa Research Journal, 98*, 81-86

Vinnikov, K.Y., Yu, Y., Rama Varma Raja, M., Tarpley, D., & Goldberg, M.D. (2008). Diurnal ‐ seasonal and weather ‐ related variations of land surface temperature observed from geostationary satellites. *Geophysical Research Letters, 35*

Wan, Z., & Dozier, J. (1996). A generalized split-window algorithm for retrieving land-surface temperature from space. *IEEE Transactions on Geoscience and Remote Sensing, 34*, 892-905

Wan, Z.M., & Li, Z.L. (1997). A physics-based algorithm for retrieving land-surface emissivity and temperature from EOS/MODIS data. *IEEE Transactions on Geoscience and Remote Sensing, 35*, 980-996

Wang, H., Yu, Y., Yu, P., & Liu, Y. (2019). Land surface emissivity product for NOAA JPSS and GOES-R missions: Methodology and evaluation. *IEEE Transactions on Geoscience and Remote Sensing, 58*, 307-318

Wang, K., & Dickinson, R.E. (2013). Global atmospheric downward longwave radiation at the surface from ground‐based observations, satellite retrievals, and reanalyses. *Reviews of Geophysics, 51*, 150-185

Wang, K., & Liang, S. (2009). Estimation of daytime net radiation from shortwave radiation measurements and meteorological observations. *Journal of Applied Meteorology and Climatology, 48*, 634-643

Wang, T., Shi, J., Ma, Y., Letu, H., & Li, X. (2020). All-sky longwave downward radiation from satellite measurements: General parameterizations based on LST, column water vapor and cloud top temperature. *ISPRS Journal of Photogrammetry and Remote Sensing, 161*, 52-60

Wu, P., Yin, Z., Zeng, C., Duan, S.-B., Gottsche, F.-M., Li, X., Ma, X., Yang, H., & Shen, H. (2021). Spatially Continuous and High-Resolution Land Surface Temperature Product Generation: A Review of Reconstruction and Spatiotemporal Fusion Techniques. *IEEE Geoscience and Remote Sensing Magazine*

Wu, P.H., Yin, Z.X., Yang, H., Wu, Y.L., & Ma, X.S. (2019). Reconstructing Geostationary Satellite Land Surface Temperature Imagery Based on a Multiscale Feature Connected Convolutional Neural Network. *Remote Sensing, 11*

Xia, Y., Peter‐Lidard, C.D., Huang, M., Wei, H., & Ek, M. (2015). Improved NLDAS‐2 Noah‐simulated hydrometeorological products with an interim run. *Hydrological Processes, 29*, 780-792

Xing, Z., Li, Z.-L., Duan, S.-B., Liu, X., Zheng, X., Leng, P., Gao, M., Zhang, X., & Shang, G. (2021). Estimation of daily mean land surface temperature at global scale using pairs of daytime and nighttime MODIS instantaneous observations. *ISPRS Journal of Photogrammetry and Remote Sensing, 178*, 51-67

Xu, S., & Cheng, J. (2021). A new land surface temperature fusion strategy based on cumulative distribution function matching and multiresolution Kalman filtering. *Remote Sensing of Environment, 254*, 112256

Yang, G., Sun, W., Shen, H., Meng, X., & Li, J. (2019). An Integrated Method for Reconstructing Daily MODIS Land Surface Temperature Data. *IEEE Journal of Selected Topics in Applied Earth Observations and Remote Sensing, 12*, 1026-1040

Yao, Y., Liang, S., Cheng, J., Liu, S., Fisher, J.B., Zhang, X., Jia, K., Zhao, X., Qin, Q., Zhao, B., Han, S., Zhou, G., Zhou, G., Li, Y., & Zhao, S. (2013). MODIS-driven estimation of terrestrial latent heat flux in China based on a modified Priestley–Taylor algorithm. *Agricultural and Forest Meteorology, 171-172*, 187-202

Yoo, C., Im, J., Cho, D., Yokoya, N., Xia, J., & Bechtel, B. (2020). Estimation of all-weather 1 km MODIS land surface temperature for humid summer days. *Remote Sensing, 12*, 1398

Yoo, C., Im, J., Park, S., & Quackenbush, L.J. (2018). Estimation of daily maximum and minimum air temperatures in urban landscapes using MODIS time series satellite data. *ISPRS Journal of Photogrammetry and Remote Sensing, 137*, 149-162

Yu, P., Yu, Y., Rao, Y.D., Liu, Y., & Wang, H. (2018). Status of the GOES-R Land Surface Temperature Product. In, *AGU Fall Meeting 2018*: AGU

Yu, W., Ma, M., Wang, X., & Tan, J. (2014). Estimating the land-surface temperature of pixels covered by clouds in MODIS products. *Journal of Applied Remote Sensing, 8*, 083525

Yu, Y., Tarpley, D., Privette, J.L., Goldberg, M.D., Raja, M.R.V., Vinnikov, K.Y., & Xu, H. (2008). Developing algorithm for operational GOES-R land surface temperature product. *IEEE Transactions on Geoscience and Remote Sensing, 47*, 936-951

Yu, Y., & Yu, P. (2018). GOES-R Land Surface Temperature Product and Its Readiness to Users. In, *10th International Conference on Urban Climate/14th Symposium on the Urban Environment*: AMS

Yu, Y., & Yu, P. (2020). Land surface temperature product from the GOES-R series. *The GOES-R Series* (pp. 133-144): Elsevier

Yu, Y., Yu, P., & Daniels, J. (2019). Production, monitoring and evaluation of GOES-R series land surface temperature data (Conference Presentation). In, *Remote Sensing for Agriculture, Ecosystems, and Hydrology XXI* (p. 111491A): International Society for Optics and Photonics

Zakšek, K., & Oštir, K. (2012). Downscaling land surface temperature for urban heat island diurnal cycle analysis. *Remote Sensing of Environment, 117*, 114-124

Zeng, C., Long, D., Shen, H., Wu, P., Cui, Y., & Hong, Y. (2018). A two-step framework for reconstructing remotely sensed land surface temperatures contaminated by cloud. *ISPRS Journal of Photogrammetry and Remote Sensing, 141*, 30-45

Zeng, Q., Cheng, J., & Dong, L. (2020). Assessment of the Long-Term High-Spatial-Resolution Global LAnd Surface Satellite (GLASS) Surface Longwave Radiation Product Using Ground Measurements. *IEEE Journal of Selected Topics in Applied Earth Observations and Remote Sensing, 13*, 2032-2055

Zhan, W., Chen, Y., Zhou, J., Wang, J., Liu, W., Voogt, J., Zhu, X., Quan, J., & Li, J. (2013). Disaggregation of remotely sensed land surface temperature: Literature survey, taxonomy, issues, and caveats. *Remote Sensing of Environment, 131*, 119-139

Zhan, W., Zhou, J., Ju, W., Li, M., Sandholt, I., Voogt, J., & Yu, C. (2014). Remotely sensed soil temperatures beneath snow-free skin-surface using thermal observations from tandem polar-orbiting satellites: An analytical three-time-scale model. *Remote Sensing of Environment, 143*, 1-14

Zhang, T., Zhou, Y., Zhu, Z., Li, X., & Asrar, G.R. (2022). A global seamless 1 km resolution daily land surface temperature dataset (2003–2020). *Earth System Science Data, 14*, 651-664

Zhang, X., Pang, J., & Li, L. (2015a). Estimation of land surface temperature under cloudy skies using combined diurnal solar radiation and surface temperature evolution. *Remote Sensing, 7*, 905-921

Zhang, X., Zhou, J., Liang, S., & Wang, D. (2021). A practical reanalysis data and thermal infrared remote sensing data merging (RTM) method for reconstruction of a 1-km all-weather land surface temperature. *Remote Sensing of Environment, 260*, 112437

Zhang, X.Y., Pang, J., & Li, L.L. (2015b). Estimation of Land Surface Temperature under Cloudy Skies Using Combined Diurnal Solar Radiation and Surface Temperature Evolution. *Remote Sensing, 7*, 905-921

Zhang, X.Y., Wang, C.G., Zhao, H., & Lu, Z.H. (2017). Retrievals of all-weather daytime land surface temperature from FengYun-2D data. *Optics Express, 25*, 27210-27224

Zhi-xia, W., Zhuo-tong, N., & Lin, Z. (2011). The Applicability of MODIS Land Surface Temperature Products to Simulating the Permafrost Distribution over the Tibetan Plateau [J]. *Journal of Glaciology and Geocryology, 1*

Zhou, J., Chen, Y., Zhang, X., & Zhan, W. (2013). Modelling the diurnal variations of urban heat islands with multi-source satellite data. *International Journal of remote sensing, 34*, 7568-7588

Zhou, J., Liang, S., Cheng, J., Wang, Y., & Ma, J. (2018). The GLASS land surface temperature product. *IEEE Journal of Selected Topics in Applied Earth Observations and Remote Sensing, 12*, 493-507

Zhou, W., Peng, B., & Shi, J. (2017). Reconstructing spatial–temporal continuous MODIS land surface temperature using the DINEOF method. *Journal of Applied Remote Sensing, 11*, 046016

Zou, D., Zhao, L., Sheng, Y., Chen, J., Hu, G., Wu, T., Wu, J., Xie, C., Wu, X., Pang, Q., Wang, W., Du, E., Li, W., Liu, G., Li, J., Qin, Y., Qiao, Y., Wang, Z., Shi, J., & Cheng, G. (2017). A new map of permafrost distribution on the Tibetan Plateau. *The Cryosphere, 11*, 2527-2542